Intense aqueous alteration on C-type asteroids: perspectives from giant fine-grained micrometeorites [**GCA-D-18-00805**]

Suttle, M.D.[1,2,3](*corresponding author*), Folco, L.[1], Genge, M.J.[2,3], Russell, S.S.[3], Najorka, J.[3]., van Ginneken, M.[4,5,6]. – martindavid.suttle@dst.unipi.it, luigi.folco@unipi.it, m.genge@ic.ac.uk, sara.russell@nhm.ac.uk, j.najorka@nhm.ac.uk, matthias.van.ginneken@ulb.ac.be

[1.]Dipartimento di Scienze della Terra, Università di Pisa, 56126 Pisa, Italy
[2.]Department of Earth Science and Engineering, Imperial College London, South Kensington, London, SW7 2AZ, UK
[3.]Core research laboratories, Department of Earth Science, The Natural History Museum, Cromwell Rd, London SW7 5BD, UK
[4.]Analytical and Environmental Chemistry (ANCH), Vrije Universiteit Brussel, Av. F.D. Roosevelt 50, 1050 Brussel, Belgium.
[5.]Laboratoire G-Time, Université Libre de Bruxelles, Franklin Rooseveltlaan 50, 1050 Bruxelles, Belgium
[6.]Royal Belgian Institute of Natural Sciences, Rue Vautier 29, 1000 Bruxelles, Belgium

Abstract

This study explores the petrology of five giant (>400µm) hydrated fine-grained micrometeorites from the Transantarctic Mountain (TAM) micrometeorite collection. For the first time, the extent and mechanisms of aqueous alteration in unmelted cosmic dust are evaluated and quantified. We use a range of criteria, previously defined for use on hydrated chondrites, including phyllosilicate fraction, matrix geochemistry and micro textures. Collectively, these micrometeorites represent ~2.22mm^2 of intensely altered hydrated chondritic matrix (with petrologic subtypes of <1.2 in the scheme of Howard et al., [2015]) and reveal a range of alteration styles. Two particles are found to contain pseudomorphic chondrules with thick fine-grained rims, while another micrometeorite contains several aqueously altered CAIs. Their outlines range from well-defined to indistinct, demonstrating that the advanced stages of aqueous alteration progressively remove evidence of coarse-grained components. The remaining two micrometeorites entirely lack coarse-grained components but are similarly altered. Thus, the combined chondrule-to-matrix ratio among these giant micrometeorites is extremely low (6.45 area%), and significantly below the average ratio found in typical CM or CR chondrites (~20%, Weisberg et al., 2006). Our findings are consistent with previous analyses from smaller Antarctic micrometeorites, which suggest that chondrules (and CAIs) derived from hydrated carbonaceous chondrite parent bodies are underrepresented among the micrometeorite flux, even when considering contributions from coarse-grained micrometeorites. Therefore, to explain the relative paucity of anhydrous material, we propose that the flux of fine-grained micrometeorites is primarily derived from intensely aqueously altered, primitive C-type asteroids, which have lost the majority of their refractory coarse-grained components by replacement with secondary phyllosilicate minerals.

1. Introduction

The interaction between liquid water and solid nebular condensates is termed aqueous alteration and represents a critical process of the early solar system's evolution. Alteration known to have occurred independently on numerous small bodies (Trigo-Rodriguez et al., 2006; Elmaleh et al., 2015) and potentially, even within the nebular itself, where grain aggregates, containing water-ice, were heated by the Sun, from passing shock waves or by other transient mechanisms (Metzler et al., 1992; Ciesla et al., 2003).

Most primitive extraterrestrial materials, including ordinary chondrites (Doyle et al., 2015), carbonaceous chondrites (Rubin et al., 2007; Harju et al., 2014; King et al., 2015), micrometeorites (Genge et al., 1997; Suttle et al., 2017a), interplanetary dust particles (Rietmeijer, 1991) and cometary dust (Zolensky et al., 2006; Noguchi et al., 2017) show evidence of aqueous alteration. However, this is most advanced, and most extensively studied, among the hydrated carbonaceous chondrite group (containing the CM and CI chondrites as well as a significant fraction [~70%, Harju et al., 2014] of the CR chondrites). These meteorites are dominated by secondary minerals, formed during alteration and contain between 2 and 20wt% water (Tonui et al., 2003; Rubin et al., 2007), primarily this is structural water held inside hydrated phyllosilicate minerals. Both the CM and CI chondrites are dominated by a complex, mixed assemblage of interlocking Fe and Mg-phyllosilicate (Tomeoka and Buseck, 1985; Browning et al., 1996), representing multiple generations of secondary mineral growth (Elmaleh et al., 2015; Lee et al., 2012; 2013). They also contain accessory Fe-Mg-Ca carbonates, minor Fe-oxides and dispersed hydrated Fe-Ni sulfides (Weisberg et al., 2006; Howard et al., 2009; 2015; King et al., 2015). Relict, anhydrous mafic silicate crystals (typically Mg-rich olivine and pyroxene grains) may be preserved, commonly as isolated matrix grains or grain clusters, representing the incompletely transformed remnants of chondrules, CAIs (Ca-Al inclusions) and AOAs (amoeboid olivine aggregates) (Hanowski et al., 2001; Velbel et al., 2012; Pignatelli et al., 2016).

In addition to disequilibrium mineral assemblages and complex alteration chronologies, the extent of aqueous alteration among the hydrated chondrite population is highly variable (Rubin et al., 2007; Harju et al., 2014; Howard et al., 2015). In general, CI chondrites are more extensively altered and are composed almost entirely of hydrated fine-grained matrix (King et al., 2015), while most CM chondrites are less-altered and retain some anhydrous components (between 5-32 vol% and typically around 25 vol%, Howard et al., 2009; 2015). However, increasingly a population of extensively altered CM chondrites, with alteration degrees equivalent to their CI counterparts are being described and classified (Zolensky et al., 1996; 1997; Rubin et al., 2007; King et al., 2017). In contrast, most CR chondrites are less-altered than either the CM or CI groups (Howard et al., 2015) and, therefore, preserve the early stages of aqueous alteration in chondritic materials (Harju et al., 2014; Le Guillou et al., 2015). Variations in the extent of aqueous alteration are also observed within individual meteorites (Zolensky et al., 1997; Lee et al., 2013). This may be due to impact brecciation on the parent asteroid (Zolensky et al., 2014) but also reveals that interaction with liquid water was localized and potentially short lived (Weisberg and Huber, 2007; Bland et al., 2009; Lee and Lindgren, 2016).

1.1. Evaluating the extent of aqueous alteration in carbonaceous chondrites – Attempts to characterise the style, extent and mechanisms of aqueous alteration in hydrated chondrites have used a range of petrographic criteria including: textural features (Velbel et al., 2012; Lee and Lindgren,

2016), elemental ratios (McSween 1979; 1989; Rubin et al., 2007), modal mineralogy (Howard et al., 2009; King et al., 2017), spectroscopy (Takir et al., 2013) and isotopic signatures within various mineral phases – notably carbonates (Lee et al., 2012; 2013). This led to the development of several different aqueous alteration schemes that assign a petrologic subtype (a numerical designation) to individual meteorites, defining their degree of alteration – where lower subtypes represent more intensely altered samples.

The main effect of aqueous alteration is the progressive replacement of a parent body's primary lithology with secondary minerals. Thus, most alteration metrics attempt to measure the relative amount of replacement that has occurred within a meteorite. Geochemical metrics – which measure the composition of the fine-grained matrix therefore trace changes in the composition of the alteration fluid as new secondary minerals are precipitated. McSween (1979; 1987) noted that as alteration advances, Fe/Si ratios decrease, while Mg/Fe ratios increase. Consequently, two common geochemical metrics are commonly used when evaluating the matrix composition in hydrated chondrites. These are (1) FeO/SiO_2 wt% oxide ratios following the convention of Rubin et al., (2007) and (2) Mg/(Mg+Fe) atomic ratios (abbreviated with the symbol Mg#). Both of these geochemical trends are directly related and reflect the progressive loss of Mg-rich anhydrous silicates (olivine and pyroxene), whose subsequent donation of Mg into the fluid phase results in the precipitation of increasingly Mg-rich phyllosilicates (Browning et al., 1996; Howard et al., 2009) and later Mg-rich carbonates (Lee et al., 2014). Texturally, this corresponds to the loss of coarse-grained structural elements within the meteorite; first as chondrule glass is replaced, and later as chondrule minerals, CAIs (Ca-Al-rich inclusions), AOAs (amoeboid olivine aggregates) and isolated matrix silicates are converted into phyllosilicates (Zolensky et al., 1997; Rubin et al., 2007; Velbel et al., 2012; Lee and Lindgren, 2016). Alteration, therefore, has the general effect of homogenising the chondrite, both texturally and geochemically. However, even the most altered group, the CI chondrites, remain heterogenous at the micron to sub-micron scale, because aqueous alteration was truncated before complete homogenization was achieved (Bland et al., 2004; Howard et al., 2015). From a mineralogical perspective, the degree of aqueous alteration can be tracked and quantified simply by measuring the phyllosilicate fraction (calculated as: [total phyllosilicate/[total phyllosilicate + total anhydrous silicates]) within a sample. Although this is a relatively crude indicator of alteration extent – which lacks the high-fidelity precision achievable with other methods, such as isotopy (Lee et al., 2014; Lee and Lindgren, 2016) or through the combined use of several different metric as in Rubin et al., (2007) – it is possible, using only the phyllosilicate fraction, to compare the degree of alteration between hydrated chondrites within the CM and CR chondrite groups as well as the C2 ungrouped meteorites (Howard et al. 2015).

1.2. Comparative studies on fine-grained micrometeorites – Many studies have revealed strong geochemical, mineralogical, textural and isotopic affinities between micrometeorites and hydrated carbonaceous chondrites. For example, Alexander et al., (2002), Genge et al. (1997) and Taylor et al., (2012) each demonstrated that the bulk compositions of most fine-grained micrometeorites show a close relationship to that of CM chondrites, while Kurat et al., (1991) and van Ginneken et al. (2012) matched the mineralogy and trace element geochemistry of several large chondritic micrometeorites to known meteorite groups, including CM and CI chondrites. Furthermore, Suavet et al. (2010) analysed oxygen isotopes in large (>500μm) particles and revealed that the majority (~50%) of these micrometeorites have signatures which directly relate them to the joint CM-CR isotopic group.

Alternatively, micrometeorites may originate from parent bodies which are related to, but distinct from the established CM/CR/CI carbonaceous chondrite groups. This argument is supported by subtle differences between the two groups, including: an apparent lack of chondrules among the fine-grained micrometeorite population (Engrand and Maurette, 1997; Reshma et al., 2013), higher olivine/pyroxene ratios in micrometeorites than chondrites, as well as a lack of carbonate and sulfate phases (Kurat et al., 1994). Micrometeorites also have unique organic signatures, containing higher CH_2/CH_3 ratios and lower carbonyl abundances than chondrites (Battandier et al., 2018) as well as trace element compositions of their olivine and pyroxene grains which extend outside the compositional ranges observed for silicates in established carbonaceous chondrite groups (Steele, 1992).

Although aqueous alteration has been extensively researched within the hydrated chondrites, comparable studies focusing on the extent of aqueous alteration in fine-grained micrometeorites are notably absent and this limits our ability to confidently answer the question: do fine-grained micrometeorites originate from the same parent bodies as CM, CR and CI chondrites, or are micrometeorites sourced from distinct parent asteroids? The absence of studies investigating aqueous alteration in fine-grained micrometeorites is most likely a product of two main limitations:

(1) ***The small size of micrometeorites*** – which are typically <200µm (Taylor et al., 2000) and always <3000µm (Suavet et al., 2009) – this means that all micrometeorites will be unrepresentative samples of their parent body's geology (Genge et al., 2008). The minimum size necessary for a representative sampling of coarse-grained components in chondritic material was quantified by Hezel et al., (2008), who calculated that extremely large surface areas, >2500mm^2, are needed. Thus, all micrometeorites and most small meteorite chips suffer sampling biases. Although, this problem is inherent in any study of micrometeorites, sampling bias may be partially overcome either through the analysis of many individual particles, or where larger samples, which are significantly more representative than their smaller counterparts are studied.
Here, we provide the first data on aqueous alteration in giant fine-grained micrometeorites, whose exposed surface areas (0.21-1.15mm^2) are sufficiently that coarse-grained structural components, such as CAIs, AOAs and chondrules are expected to be found. However, despite their larger size, the conclusions drawn from these micrometeorites should be considered along with existing data from small micrometeorites and larger hydrated carbonaceous chondrites, thereby providing a more comprehensive view of the flux of hydrated chondritic material to Earth.

(2) The ***effects of terrestrial overprints***, including atmospheric entry heating and terrestrial weathering also overprint a particle's parent body petrography. Flash heating during atmospheric entry significantly alters the mineralogy and textures of most micrometeorites (Suttle et al., 2017a). Even among unmelted micrometeorites, the hydrated phyllosilicate matrix has typically experienced dehydration, dehydroxylation or recrystallization at sub-solidus temperatures during entry. Meanwhile, at the micrometeorite's margin, localized melting and degassing occurs resulting in the formation of igneous and magnetite rims (Genge, 2006) and, in extreme cases, particle fragmentation (Suttle et al., 2018). By contrast, terrestrial weathering leads to leaching, dissolution and replacement of parent body minerals with hydrated, S, K and Cl-rich phases, such as jarosite and halite and calcite (van Ginneken et al., 2016). The effects of these later geological processes must be understood before a sample's parent body geology can be analysed.

In this study, we characterise the petrography of five giant fine-grained micrometeorites and evaluate their degree of aqueous alteration. This provides new data on the relationship between micrometeorites and known carbonaceous chondrite groups, whilst also expanding the discussion of aqueous alteration on primitive C-type asteroids to include perspectives from the micrometeorite flux. This study therefore complements existing studies based on smaller (<100µm) micrometeorites and their larger C2/C1 hydrated meteorite counterparts.

2. Samples

Micrometeorites recovered from loose sediments on the summit plateaus of the Transantarctic Mountains represent a unique collection of cosmic dust, characterised by abundant large (>500µm) micrometeorites (Suavet et al., 2009). This contrasts with the size distributions from all other Antarctic, deep-sea and fossil micrometeorite collections that are dominated by small particles (<600µm and typically <150µm, Taylor et al., 2000; Suavet et al., 2009; Suttle et al., 2017b). The advantage of studying such large micrometeorites, lies in the ability to analyse a more representative sample of their parent asteroid and, therefore, to draw more reliable conclusions about the provenance and geological history of individual particles.

The estimated total accumulation duration for the TAM micrometeorite collection lies between 1-3Ma. This is constrained by the presence of Australasian microtektites, with a formation age of ~0.78Ma (Folco et al., 2008), by the presence of cosmic spherules with a thermal remnant magnetization signature acquired during the Earth's reversed polarity field, also >0.78Ma ago (Suavet et al., 2011), and from ^{10}Be, bedrock exposure ages, measured on the terrestrial collection surface (~4.4Ma, Welten et al., 2008). Such long time periods are necessary for the accumulation of rare, large micrometeorites (Suavet et al., 2009). However, long residence times exposed above the ice sheets, have also resulted in significant terrestrial weathering (van Ginneken et al., 2016; Genge et al., 2018). Consequently, most TAM micrometeorites have encrustations and secondary replacement with jarosite, calcite and halite minerals, which progressively overprint their parent body and atmospheric signatures (van Ginneken et al., 2016).

We selected five of the largest, fine-grained micrometeorites (460-1000µm, TAM19B-7, TAM19B-17, TAM19B-18, TAM15-11 and TAM66-1) which were obtained from sediment traps, located on the nunatak Miller Butte [72°42.078' S, 160°14.333' E, at an elevation of ~2600m]. Some of these particles were previously analysed in two previous publications by Suttle et al., (2017a; 2018), which focused on the petrographic evolution of fine-grained micrometeoroids during atmospheric entry heating. However, in this study we, instead, investigate the pre-atmospheric, parent body properties of these samples, specifically looking at aqueous alteration on their parent asteroids.

3. Methods

Our micrometeorites were analysed primarily at the Natural History Museum (NHM), London in the Imaging and Analysis Centre. Particles were investigated using a range of microanalysis techniques, including: back-scatter electron imaging (BEI), electron microprobe analysis (WD-EMPA), standard-based SEM-EDS, elemental X-ray mapping and micro X-ray diffraction (µXRD). Later, at the University of Pisa, Italy we also collected high-resolution BEI and standard-less EDS data on two particles: TAM66-1 and fragments from TAM19B-7. Table.1 displays the analysis types performed on each sample.
For a single particle, TAM19B-7, we also conducted a petrofabrics analysis to investigate the

relationship between aqueous alteration and shock deformation. After which we extracted TAM19B-7 from the epoxy resin, crushed the particle and re-embedded 10 fragments (~50-300µm in size) for further analysis. In addition, we have preserved the remaining particle's mass (~0.5mg) for a planned future O-isotope study. By fragmenting this micrometeorite and analysing several random chips we are able to explore significantly more of the particle's petrography and, therefore, achieve a more representative analysis of the micrometeorite.

3.1 Geochemistry and mineralogy – Geochemical data were collected using either a Cameca SX100 SEM – a WD-EMPA system, a Zeiss SEM-EVO 15LS fitted with an Oxford Instruments' 80mm^2 X-Max silicon drift detector (SSD) energy dispersive spectrometer (EDS), providing standard-based geochemical assays or a FEI Quanta 450 field emission SEM, equipped with a Bruker Quantax 400 XFlash detector [with a 129eV spectral resolution], which provided standard-less EDS data.

For the Cameca, WDS analyses were performed under acceleration voltages of 20kV, beam currents of 10nA and a focused beam spot (<1µm diameter). The system was calibrated, prior to use, with a suite of mineral standards, specific to each element under detection. Eleven elements, commonly found in silicate minerals were included in the pre-defined element list, with oxygen calculated by stoichiometry. After analysis, the in-house Cameca PAP matrix correction software was used to remove artefacts arising from atomic number, absorption and secondary fluorescence effects. Elemental detection limits for this instrument are on the order of 0.02-0.05wt% and elemental uncertainties vary between 0.01-0.03wt%.

For the standard-based EDS system [Zeiss EVO], data were collected under acceleration voltages of 20kV, beam currents of 3nA and a focused beam spot (~1µm diameter). Pre-analysis gain calibrations were performed on an elemental cobalt standard, while routine monitoring of beam current, count deadtimes, acceleration voltages and sample-detector distance ensured ideal conditions were maintained throughout data collection. Post-acquisition processing used the Oxford Instruments INCA software. Weight totals were calculated using "oxygen by stoichiometry" which assumes that all cations occupy their lowest oxidation states. Elemental detection limits are on the order of 0.2wt% and analytical uncertainties vary between 0.1-0.5wt%.

A FEI Quanta 650 FEG-SEM, located at the NHM and fitted with a Bruker Flat Quad 5060F EDS detector plate was used to collect BEI data as well as high spatial resolution quantitative X-ray element maps. These were generated using a 12kV beam which rastered over the micrometeorite cross-sections for 2-24hours. Count rate of 27.7kcps and deadtimes between 5-10% were maintained throughout acquisition.

A Rigaku Rapid II micro-diffraction system, containing a 2D curved imaging plate detector, a Cu X-ray source, a collimator pinhole system and adjustable goniometer head were employed to collect diffraction data. A 100µm beam spot was used and samples ran for approximately 20 hours, during this time the micrometeorite cross section, embedded in epoxy resin, were held at a constant ω angle (20º2θ) but continuously rotated in the φ axis. Peak positions in the converted 1D patterns were identified by comparison against a comprehensive mineral standards database (PDF-4 database from ICDD).

More detailed information for each of the analytical procedures and their operating conditions can be found in Suttle et al., (2017a; 2018).

3.2. 2D shock fabric analysis – All five micrometeorites were analysed with a 2D image analysis procedure, that evaluates the orientations of void space within a fine-grained micrometeorite's matrix. This was investigated by extracting and measuring the area and direction of each void's long-axis with respect to an arbitrary reference 'north'. The minimum void size analysed was set at a threshold of 50µm^2. Smaller voids were ignored since these were composed of relatively few pixels. Void orientations were binned by 10° increments and used to generate circular histograms (rose diagrams) from which the presence or absence of a petrofabric could be determined. Rose diagrams were evaluated quantitatively using entropy calculations to determine the degree of disorder. A lower entropy value reflects a mature fabric with a well-defined alignment of voids, while randomly orientated voids generate an isotropic (uniform circular) rose diagram and, therefore, a high entropy. Additional details of this data processing procedure can be found in Suttle et al., (2017b) whose technique was followed in this study. In addition, the entropy values of the CM chondrites (Cold Bokkeveld and Jbilet Winselwan) also analysed in Suttle et al., (2017b) are employed in this study to provide context to the entropy value calculated from the giant TAM micrometeorites.

4. Results

4.1. General characteristics – All five particles have characteristic textural and petrographic features that identify them as unmelted, fine-grained micrometeorites. These include partial or complete magnetite rims, igneous rims, vesicles, Ni-bearing forsterite (seen in 4 of 5 particles), abundant Mg and Fe-bearing phyllosilicates, in the form of intergrown clusters or clumps (which are now seen as amorphous dehydration products and identified by the presence of dehydration cracks) and accessory Fe-Ni metal and Fe-oxides (Figs.1-5 in this manuscript may be compared with micrometeorites shown in Genge et al. [2008]).

The TAM micrometeorites also have similar compositions (Fig.6, Table.2), characterised by chondritic abundances for Al, Ti, Si, V, Cr, P, Mn, Cu, Na and S and depletions, up to 1 order of magnitude below CI Ivuna, for Ca, Mg, Ni, Co and Zn. In the case of Mg, depletions vary between 0.16-0.61x below CI values. Conversely, mild enrichments are seen for Fe, between 1.4-2.2x, while all micrometeorites also contain significantly elevated K concentrations (>10.9x), which in TAM51.11 reach up to 35x CI values. Deviations from chondritic concentrations are primarily a product of terrestrial weathering, where long residence times in the Antarctic environment have resulted in the leaching and dissolution of soluble phases, the alteration of glass and the formation of secondary minerals such as jarosite, akaganéite, palagonite, (Mg,Fe)-oxyhydroxides, calcite and halite (van Ginneken et al., 2016). Terrestrial alteration by jarosite replacement is common in the TAM micrometeorites and forms thick encrustation rims, which are notable on TAM19B-17 (Fig.2). Akaganéite was also identified as a major phase in the µXRD pattern of TAM19B-7 (Fig.7). This mineral forms where FeNi-sulfides (pyrrhotite, troilite and tochilinite) are altered in the presence of Cl -bearing water and is, therefore, a common component of weathered Antarctic meteorites (Bland et al., 1997).

4.2. TAM19B-7

4.2.1. Main cross-section – This particle is the largest unmelted, fine-grained micrometeorite analysed to date. The main cross-sectioned surface (Fig.1A-D) has a rectangular shape, with dimensions of ~830x950µm and an exposed surface area of 0.69mm^2. The particle's matrix is highly vesicular, suggesting that this micrometeorite is transitional between the fine-grained and scoriaceous class, reflecting the effects of partial melting during atmospheric entry. However, relict textures show that

290 the pre-atmospheric matrix was compact, dense and fine-grained, being composed of phyllosilicates
291 (with a high phyllosilicate fraction of 0.97) and with minimal coarse-grained PCP clumps. The most
292 distinctive feature of this particle is the presence of two geochemically distinct domains, separated by
293 a relatively sharp compositional contact (with a boundary thickness of ~5µm). The lower left portion
294 of the micrometeorite contains Mg at concentrations between 4.1-8.2wt% and Fe at concentrations
295 between 12.4-20.9wt%, while the upper right domain is heavily depleted in Mg, with concentrations
296 below 3.0wt%. However, Fe concentrations in this region is high, varying between 16.0wt% and
297 31.9wt%. These two domains are, therefore, Mg-bearing (Mg#26-60) and Fe-rich (Mg#0-36)
298 respectively. In the upper right portion, the majority of large voids (vesicles, dehydration cracks and
299 interconnected networks formed from both void types [Suttle et al., 2018]) have Fe-rich linings, while
300 Fe-rich linings are less pronounced in the Mg-bearing domain.

301 Within the Fe-rich domain there is a rounded elliptical region of matrix with dimensions of
302 approximately 180x140µm and an average diameter of ~160µm (Fig.1B, aspect ratio of ~1.3). This
303 component is geochemically indistinguishable from the host micrometeorite, but clearly identifiable
304 under BEI due to its distinctive matrix texture. This object is mantled by a fine-grained, weakly layered
305 and compact rim with variable thickness, between 10-25µm. The inclusion core has an abundance of
306 rounded voids (<20µm diameter), which results in a high porosity. Several of these voids are coated
307 with Fe-rich rims (Suttle et al., 2018).

308 **4.2.2 Additional fragments** – We subsequently crushed TAM19B-7 and analysed the resulting
309 fragments (some of which are shown in Fig.1E-H). The exposed cross-sectional areas of these
310 fragments are smaller, ranging from 0.01-0.12mm^2. However, these chips effectively increase the total
311 area of analysis by 40% and provide a 3D perspective of the particle interior. Two of the fragments
312 shown in Fig.1 (E and H) are orientated at 90° to the original cross-section (shown in Fig.1A-D) and
313 include the flat, polished surface of the initial section on one edge – these are marked by a dashed
314 green line. Despite increasing the area for analysis, we did not find additional unambiguous coarse-
315 grained components, although two fragments (Fig.1G and 1H) with faint rounded outlines were
316 observed and these may represent additional inclusions.

317 **4.3. TAM19B-17** – This micrometeorite has a triangular cross-section, with maximum dimensions of
318 460x480µm and a total exposed surface area of 0.21mm^2 (Fig.2A.). The phyllosilicate matrix is
319 heterogenous, fine-grained, Fe-rich (avg Mg#18) and dense, containing limited pore space. Significant
320 variations in back scatter potential (between Mg#3-38) produce a complex texture of intergrown or
321 amorphous phases. For example, dark, poorly defined and dense regions of relatively Mg-rich matrix
322 (Mg>6wt%) are sparse and mantled or cross-cut by large clusters of lighter, Fe-enriched (Mg<3wt%,
323 Fe>20wt%) and coarser-grain material, which may contain several small dehydration cracks. The
324 calculated phyllosilicate fraction for this micrometeorite is 0.96. Micron scale veins and infilled pores
325 are also identified (Fig.2E).

326 Anhydrous silicates in TAM19B-17 are relatively common and appear as large (>80x100µm) forsterite
327 crystal clusters with anhedral morphologies. Grains may enclose small (<4µm diameter) Fe-Ni metal
328 droplets or are surrounded by thin (<5µm) Fe-Ni sulfide linings. Most silicate crystals are heavily
329 altered and replaced, as evidenced by their rounded outlines (Fig.2E). Several grains have broken into
330 a series of smaller residual silicate crystals or contain fractures. Silicate margins are also surrounded
331 by thick (>20µm) Fe-rich growths. In Fig.2A the outlines of three prominent refractory crystal clusters
332 have been traced. They have rounded, elongate and oval-shaped morphologies. These regions

typically have darker greyscale colours (low Z values) representing Mg-enriched matrix in between the crystal fragments.

TAM19B-17 also has several combined Ca, Al and Ti hotspots (Fig.2C). Four such zones of enrichment are identified, the largest of which is shown in Fig.2D and exceeds 100µm in diameter. The core of this hotspot contains small Al-spinels embedded within a porous material, which we tentatively identify as bridgmanite - a silicate perovskite composed of ferromagnesian silicates [$(Mg,Fe)SiO_3$] and calcium silicate [wollastonite, $CaSiO_3$], and whose combined stoichiometry approaches $(Mg,Fe,Ca)(Al,Si)O_3$) (Table.2, B1-3). This core of this inclusion is surrounded by a thick and equally porous margin of more Fe-enriched material with a stoichiometry closer to that of an Al-rich pyroxene.

4.4. TAM19B-18 – This micrometeorite has an elongated and irregular cross-section, with dimensions of 870x530µm and a total exposed surface area of 0.27mm^2 (Fig.3A). The particle is dominated by large (>80µm) clusters of coarse, Fe-rich phyllosilicates (Mg#20-44, ~3-9wt% Mg) which are identified by their prominent internal and subparallel dehydration crack sets (Fig.3E and F) and relatively sharp compositional boundaries. These coarse phyllosilicate clumps represent up to 85% of the particle's exposed surface area, giving this particle a high calculated phyllosilicate fraction of 0.93. The remaining regions, seen in cross-section, are either pore space, which is primarily in the form of large and interconnected cracks (Suttle et al., 2018), or isolated anhydrous silicates (Fig.3B, C and E). The compositions of olivine crystals varies between Fo22-98 and in size between~<5-120µm. Most silicate grains contain penetrating fractures that are infilled by thin serpentine veins (Fig.3C). Thick phyllosilicate mantles also wrap around most crystals (Fig.3B), producing overgrowth rims that have a weakly foliated texture.

This micrometeorite also contains an embedded clast (~130x180µm, Fig.3A) characterised by a compact, mildly Mg-enriched matrix (Mg#39-49, ~7-9wt% Mg) and contains a single large (35x40µm) olivine crystal. Sub-spherical micron-scale Fe-oxide beads are also present in the matrix, prior to atmospheric entry, these were most likely tochilinite grains or Fe-oxides.

4.5. TAM15-11 – This micrometeorite has an irregular, broadly triangular cross-section with dimensions of approximately 1000x470µm and a total exposed surface area of ~0.30mm^2 (Fig.4A). The particle margin has a well-developed but discontinuous magnetite rim and localised portions of igneous rim. Meanwhile, the particle interior is primarily composed of (dehydroxylated) coarse-grained Fe-rich (Mg# 2-46%, 0.2-8.3wt% Mg) phyllosilicate clusters (Fig.4A and 4E), which contain large sub-parallel dehydration crack sets and finer-grained Mg-enriched zones (Fig.4G). The coarse phyllosilicate clusters have irregular, elongated or lozenge shapes and reach up to ~300µm in length. Anhydrous silicate crystals range in size from <5µm (Fig.4D) to 80µm (Fig.4C) and compose approximately 1.5% of the particle's exposed surface area (resulting in an extremely high phyllosilicate fraction of 0.98). Most of the anhydrous silicates are pyroxenes, with both low-Ca pyroxene (En93-96, Fs2-5, Wo0-1 [as enstatite]) and high-Ca pyroxene (En49-56, Fs2-5, Wo39-46 [reflecting both augite and diopside compositions]) being common and occurring in close association (Fig.4C). By contrast, olivine is relatively rare and has a Mg-poor composition (Fo46). The anhydrous silicate crystals are collected into discrete clusters and have either sharp fractured margins and angular morphologies (Fig.4C) or smooth and rounded edges which show a distinct Fe-enrichment (Fig.4D).

4.6. TAM66-1 – This micrometeorite has a smooth fine-grained external surface (Fig.5G) and dimensions of 1000x950x720µm. In cross-section, the exposed surface area is approximately

930x740µm, equivalent to ~0.29mm^2 (Fig.5A). The particle margin supports a well-developed but discontinuous magnetite and igneous rim, which is broken in several places along the top and right sides (Fig.5A). These fractures are assumed to form whilst on the Earth's surface as a result of weathering and transport. Fractures also cut through the particle interior, following the margins of inclusions (Fig.5C and F) and the boundaries between larger anhydrous silicate crystals and fine-grained matrix, as shown in Fig.5E.

The micrometeorite's interior contains several distinct regions of fine-grained Fe-poor/Si-rich matrix which are surrounded by thick mantles of (dehydroxylated) Fe-rich phyllosilicates with a vesicular texture. This is demonstrated in Fig.5C and 5F, where two approximately circular inclusions, with dimensions of 280x200µm and 90x80µm respectively are present. They both have thick rims with variable widths (40-100µm and 30-40µm respectively), while the inclusion cores contain a compact zone composed of Mg-depleted (1.5-3.4wt%, ~Mg#10-30) dark matrix which has several small (5-15µm) rounded, residual anhydrous silicate crystals, with predominantly low-Ca pyroxene compositions (En60-66, Fs34-38, Wo<2). Likewise, the remainder of the particle's matrix is also composed of many small isolated regions with irregular shapes and well-defined margins. They have similar textural relationships defined by vesiculated Fe-rich matrix mantling residual anhydrous silicate crystals, as shown in Fig.5E – where a single Low-Ca pyroxene grain has been surrounded and partially infilled with phyllosilicate matrix or as in Fig.5D – where a region of dark matrix, containing high-Ca pyroxene is similarly enclosed.

4.7. Petrofabric analyses – The 2D image processing technique outlined in Suttle et al., (2017c) was used to evaluate the orientation of voids within the matrix of all five micrometeorites (Table.3, Fig.10). Low entropy values (S<2.783 [jbilet Winselwan]), low circular variance values (σ^2<0.3) and high kappa concentration factors (κ>0.5) indicate a well-defined preferred orientation of their internal voids and consequently strong petrofabrics, defined by the former existence of aligned phyllosilicates (Suttle et al., 2017c).

Two micrometeorites (TAM19B-7 [S=2.599] and TAM19B-17 [S=2.688]) fit these criteria. TAM19B-7 demonstrates the strongest alignment of void long-axes, which trend in an NW-SE orientation; this is broadly parallel to the flattening direction of the elliptical inclusion seen in Fig.1B. In contrast, the petrofabric in TAM19B-17 was calculated from only 48 voids, rather than several hundred, as with the other samples. Thus, due to the lower porosity of this micrometeorite, the petrofabric analysis carries a significantly lower degree of certainty. Two further micrometeorites (TAM15-11 [S=2.744] and TAM19B-18 [S=2.785]) have relatively low entropy values similar to the two shocked CM chondrite reference samples and, therefore, weaker petrofabrics, which we have defined as probable and possible respectively. In contrast, no preferred orientation of voids was detected in TAM66-1 [S=2.860].

5. Discussion

5.1. Separating terrestrial weathering from parent body features – On Earth, micrometeorites are attacked from the particle edge as terrestrial alteration migrates inwards. Because the TAM collection is the focus of the only dedicated study into the mechanics of weathering in micrometeorites (van Ginneken et al., 2016), their distinctive weathering profiles; formed in cold, acidic and subaerial environments are well-documented. As previously outlined, jarosite, halite and calcite typically form additions to particles as thick encrustations coating particle exteriors. Simultaneously, micrometeorite

interiors are slowly replaced by simple weathering products, including jarosite, akaganéite, palagonite, ferrihydrite, limonite and Al-bearing clay minerals. Here, the leaching of fluid-mobile elements commonly occurs, with the loss of Ni, Co, S being common effects. Moreover, in heavily leached particles Mg depletions occur (Kurat et al., 1994; Genge et al., 1997). Similarly, anhydrous silicates are etched by acids and dissolved leaving cavities which are later infilled. Similarly, voids such as cracks and vesicles are also progressively infilled.

Although the five micrometeorites studied here have significant weathering overprints, both geochemical (Figs.6 & 8) and textural (Fig.1-5, particle margins) their pre-atmospheric parent body textures and much of their geochemistry is well-preserved and resolvable. This is evident from the retention of broadly chondritic compositions, the preservation of subtle matrix textures, including the elliptical inclusions seen in TAM19B-7 and TAM66-1 (Figs.1B, 1C, 5C and 5F) and the overgrown phyllosilicate clusters in TAM19B-18 (Fig.3A) and TAM15-11 (Fig.4A and E). Furthermore, the survival of anhydrous silicate crystal clusters, unfilled cracks and vesicles and the existence of significant geochemical variation across each particle also support the idea of incomplete weathering, which is in contrast to the intensely weathered coarse-grained micrometeorites shown in van Ginneken et al., (2016, Figs. 4C and 4D) that have no identifiable relict textures, extremely thick (>100µm) jarosite overgrowth rims, densely layered limonite masses and homogenous back-scatter potential Z-values throughout their cross-sections.

5.2. Identifying atmospheric entry heating overprints – The formation of dehydration cracks, vesicular matrix, large rounded vesicles, interconnected channels, localized partial melting at the micrometeorite's margin and simultaneous solid-state crystallization of the particle's internal phyllosilicate matrix into (metamorphic) olivine are characteristic features and well-documented effects of atmospheric entry heating (Suttle et al., 2017a; 2018). In the five micrometeorites studied here; discontinuous magnetite rims and variable thickness igneous rims are, while the internal textures contain either abundant dehydration cracks or vesicular matrix, this requires that their pre-atmospheric phyllosilicates have experienced dehydration and dehydroxylation; releasing their water content and developing significant porosity. Despite this process, much of their parent body textures and relict anhydrous phases are preserved. This requires that partial melting was limited, suggesting that peak temperatures did not exceed 1350°C, the solidus for chondritic matrix (Toppani et al., 2001) and were likely <800°C (Suttle et al., 2017a; 2018). Further analysis of the atmospheric entry alteration in these particles can be found in Suttle et al., (2018).

5.3. Evidence for aqueous alteration – Prior to their terrestrial alteration (by both atmospheric entry [Section 5.2] and Antarctic weathering [Section 5.1]) these five micrometeorites were composed of intermixed Fe and Mg-bearing phyllosilicates, whose relict textures reveal complex clusters of coarse Fe-rich and finer-grained Mg-rich zones that overlap and cross-cut each other. Small (<5µm) anhydrous silicate crystals are still present in all the micrometeorites studied, while larger crystals (>10µm) are entirely absent from TAM19B-7 and rare in TAM15-11. These residual silicates have anhedral morphologies and are typically fractured into a series of smaller grains with smooth, rounded edges. They also commonly have thick phyllosilicate overgrowths, which may be layered (as in TAM19B-18) or homogenous (as in TAM66-1). These textures are definitive evidence of significant parent body aqueous alteration.

5.3.1. Chondrule pseudomorphs and ghost CAIs – Several rounded inclusions with elliptical or circular shapes were found in TAM19B-7 (Fig.1A-D, 1H) and TAM66-1 (Fig.5A-F). These inclusions are

approximately 100-300µm in diameter, composed of amorphous dehydroxylated phyllosilicates and Fe-oxides and mantled by compact, low porosity, fine-grained rims. In TAM66-1, the two inclusions contain many small relict anhydrous silicates (Table.2, entries 38-40) as well as rare Mg-Al spinels (Table.2, entries 41 & 42). Conversely, the inclusion cores in TAM19B-7 contain many rounded voids set within a fine-grained porous groundmass, which is geochemically indistinguishable from the host micrometeorite's matrix. Thus, the size, shape and presence of fine-grained rims in these inclusions are reminiscent of chondrules, while their mineralogy (and in TAM19B-7 internal texture) are distinct from the igneous assemblages of anhydrous silicates, FeNi metal, silicate glass and sulfides that are found in chondrules (Jones, 2012).

We interpret these inclusions as aqueously altered and subsequently flash heated chondrules. Initially, their anhydrous igneous assemblages were replaced by Mg-rich phyllosilicates during aqueous alteration, forming pseudomorphic chondrules. However, relict fragments of olivine and pyroxene found in TAM66-1 (Fig.5C and 5D) survived alteration and attest to their polymineralic anhydrous precursors. In contrast, in TAM19B-7 aqueous alteration is more advanced, resulting in the geochemical homogenisation of the pseudomorphic chondrule with the surrounding matrix. Later, during atmospheric entry, the altered chondrules experienced dehydration, dehydroxylation and volatile de-gassing, resulting in the formation of dehydration cracks, the many large rounded vesicles that dominate one of the inclusions in TAM19B-7 and the vesicular textures observed in the Fe-rich fine-grained rims (Suttle et al., 2017a; 2018). However, because atmospheric entry heating was modest, partial melting was limited and the parent body chondrule outlines and their fine-grained rims are, therefore, preserved. Modified chondrules with high porosities, amorphous mineralogies and residual phyllosilicates are relatively common, being found in abundance among the aqueously altered and thermally metamorphosed class of CM chondrites (Nakamura, 2005; Lee et al., 2016), which are increasingly considered to be an important and abundance group of parent bodies among the asteroid belt (Beck et al., 2018).

Similar coarse-grained components are present in TAM19B-17; three large (~100µm diameter) irregular shaped inclusions were identified in Figs. 2A and 2C. These inclusions are interpreted as aqueously altered refractory phases. This is because they contain elevated abundances of refractory elements, including Ca (0.3-7.9wt%), Al (1.8-5.1wt%) and Ti (0.1-0.2wt%), which are collected into small bright spots, most likely representing residual mineral grains that survived alteration. The largest refractory inclusion, shown in Fig.2D, is zoned irregular-shaped, with a porous core and radiating Fe-rich rim. Chemical analysis of the inclusion's core (Table.2, entry 10) reveal a refractory silicate composition approaching pyroxene (approximately $[Mg,Fe,Ca][Al,Si]O_3$), while the outer rim is dense, Fe-enriched (Fig.2B) and of variable thickness. Although the inclusion core retains refractory material, the margin has been entirely replaced with secondary minerals (assumed to be Fe-phyllosilicates), which grew outwards from the host inclusion. These alteration products are, therefore, analogous to the altered CAIs described from the C2 Tagish Lake meteorite by Takayama and Tomeoka (2012, Fig.10). They observe large (~300µm diameter) zoned refractory assemblages, mantled by thick Fe-rich phyllosilicate rims and whose dark cores have higher porosities, as well as residual refractory minerals (perovskite and Al-spinel). The biggest difference between these two assemblages is the presence of abundant carbonate in the Tagish Lake CAIs, which are not present in the micrometeorite's inclusion. This is because the Tagish Lake lithology is carbonate-dominated while micrometeorites have considerably less carbonate which is subsequently lost during atmospheric entry heating, even at modest peak temperatures (<600°C, Nozaki et al., 2006). However, their

removal by thermal decomposition, along with the dehydration of phyllosilicates explains the presence of rounded voids within the Fe-rich rim surrounding this inclusion (Fig.2D). Thus, the Ca-Al-Ti hotspots within TAM19B-17 are interpreted as ghost CAIs and altered olivine clusters formed by advanced aqueous alteration.

5.3.2. Aqueous alteration in *matrix-only* micrometeorites – The remaining two micrometeorites (TAM19B-18 and TAM15-11) entirely lack coarse-grained components and instead are composed of fine-grained matrix and isolated anhydrous silicates only. Variations in the back-scatter potential of their matrix, coupled with their complex intergrown texture, imply multiple generations of secondary mineral growth during aqueous alteration (Tomeoka et al., 1985; Vebel et al., 2012). In TAM15-11 several anhydrous silicate crystals have fractured morphologies, potentially indicating a fluid-assisted brecciation phase or simultaneous impact brecciation and aqueous alteration – as suggested by Zolensky et al., (1997), Rubin (2012), Hanna et al., (2015) and others. Conversely, in TAM19B-18, anhydrous silicates are rounded and have thick phyllosilicate rims. Here, serpentine veins cross cut these phyllosilicate rims (Fig.3B) and penetrate the silicate crystal's core. A stratigraphic relationship can, therefore, be established: the phyllosilicate overgrowths must predate the serpentine veining. This requires that aqueous alteration progressed initially by the growth of hydrated phyllosilicates mantles that grew around the anhydrous silicates, initially using these crystals as a substrate and replacing the original matrix, which was probably a porous mixture of amorphous Fe-rich silicate (Noguchi et al., 2017). Furthermore, because the phyllosilicate rims in TAM19B-18 are layered, this implies successive periods of growth, to develop a concentric layered texture. However, during a later alteration period serpentine veins then grew through the rim and began to consume the olivine host substrate. Similar chronologies, where anhydrous silicates are initially used as a substrate and later as source material for secondary phyllosilicate growth, are characteristic alteration mechanisms of hydrated chondrites and were previously described in Greenwood et al., (1994) and Takayama Tomeoka (2012) within Cold Bokkeveld and Tagish Lake.

5.4. Evaluating the extent of aqueous alteration in fine-grained micrometeorites – We attempt to quantify the degree of alteration affecting these giant TAM micrometeorites using two independent evaluation methods (matrix geochemistry and modal mineralogy). Both approaches support the hypothesis that these micrometeorites are intensely altered and derived from low petrologic subtype parent bodies.

5.4.1. Geochemical data – The analysis of bulk matrix geochemistry in carbonaceous chondrites is one method used for evaluating the degree of aqueous alteration. As alteration progresses, the composition of the alteration fluid evolves. Increasing Mg concentrations occur due to the dissolution of anhydrous silicate crystals, which are then re-precipitated as Mg-rich phyllosilicates (Velbel et al., 2012; Elmaleh et al., 2015). Thus, bulk matrix "FeO/SiO_2" ratios decrease (Rubin et al., 2007), while the Mg# increase (McSween 1979; 1987) as alteration advances. Therefore, the average bulk matrix composition of a sample can be used to approximate the degree of alteration.

In Fig.8 we plot both major element geochemical ratios, obtained from a variety of hydrated chondritic samples. This includes: 77 small (<100μm) Antarctic fine-grained micrometeorites, derived from the Cap Prud'homme micrometeorite collection, as well as a selection of hydrated carbonaceous chondrites (CI Ivuna and several CM2 chondrites), loaned from the NHM, London. The majority of these samples were previously analysed in Suttle et al., (2017a) and their geochemical data are included here as a supplementary file (Table.S1). In addition, we plot the bulk matrix data from our

five giant TAM micrometeorites. A linear regression trendline is plotted through the Cap Prud'homme micrometeorites. This logarithmic $[Mg\# = -25.81 \ln(\mathrm{FeO}/\mathrm{SiO_2}) + 48.19]$ line-of-best-fit demonstrates a strong negative correlation (R^2=0.86) between the Fe and Mg concentrations within a micrometeorite's matrix. This can, therefore, be viewed as a progressive aqueous alteration trend along which hydrated chondritic materials lie. More altered samples plot in the top left quadrant, at high Mg# values and low FeO/SiO_2 values.

TAM19B-18 lies close to the alteration trendline (with average values of FeO/SiO_2=1.46, Mg#=33.9) while the remaining four micrometeorites have anomalously low Mg concentrations and, therefore, plot in the lower left quadrant of Fig.8. Their low-Mg values are inconsistent with a hydrated chondritic sample and, instead, suggest that a later geochemical process has subsequently altered their matrix composition. In section 5.1 we noted that the TAM micrometeorites studied here are affected by terrestrial weathering. As a result, the bulk matrix compositions, shown in Figs.6 and 8, demonstrate depletions in Mg due to leaching and mobilisation by terrestrial fluids (Kurat et al., 1994; van Ginneken et al., 2016). However, an attempt can be made to correct for the missing Mg in these micrometeorites by using the alteration trendline, defined from the small Cap Prud'homme micrometeorites as a guide and raising the Mg# values of the intensely weathered micrometeorites until each data point plots directly on the aqueous alteration trendline. This provides an approximation of their pre-terrestrial Mg concentration and allows us to estimate their degree of alteration.

Assuming these corrected Mg# values are approximately correct; the five micrometeorites appear to span a range of alteration degrees; their relative sequence from least to most altered is: TAM19B-18<TAM19B-17<TAM66-1<TAM19B-7<TAM15-11. Furthermore, assuming distance along the alteration trendline is proportional to the degree of alteration, then TAM19B-18 appears to be significantly less-altered than the remaining four micrometeorites. Using the hydrated carbonaceous chondrites as a reference, the four most altered micrometeorites plot in a tight group and with similar positions to that of ALHA 81002, Mighei and Cold Bokkeveld. These meteorites are characterised by moderate to intense aqueous alteration histories and accordingly have been assigned low petrologic subtypes in several studies (Greenwood et al., 1994; Zolensky et al., 1997), including that of Howard et al., (2015) who classified all three meteorites with a petrologic subtype of 1.4.

In contrast, TAM19B-18 plots further down the alteration trendline and close to Jbilet Winselwan. This meteorite was previously investigated in Friend et al., (2018), who concluded that Jbilet Winselwan is only mildly altered, with a petrologic subtype between CM2.5-2.6 (on the scale of Rubin et al., [2007]). However, since this chondrite is a breccia, composed of many diverse clasts, other studies have arrived at distinctly different conclusions, as in the case of Pernet-Fisher et al., (2014) who classified Jiblet Winselwan as a CM2.0-2.3 petrologic subtype (also on the scale of Rubin et al., [2007]). Our sample of Jbilet Winselwan (P18927) has a relatively Fe-rich matrix (Mg# 39) and appears less altered than the other CM2 chondrites analysed here, suggesting a moderate degree of alteration.

5.4.2. Phyllosilicate fraction – Another method used to evaluate the degree of aqueous alteration in chondrites is modal mineralogy, developed by Bland et al., (2004) and Howard et al., (2009; 2015) and later employed for CI chondrites by King et al., (2015). This approach calculates the phyllosilicate fraction in a hydrated chondrite as a proxy for the degree of secondary mineral replacement. We calculated the approximate phyllosilicate fraction in the five TAM micrometeorites using their exposed cross-sections to determine major mineral abundances. For each particle their high-resolution BSE images and EDX maps were used to identify the abundance of phyllosilicates and anhydrous silicates

as a percentage of the particle's total surface area (their calculated phyllosilicate fractions are shown in Table.1). Using the single element Mg-Kα EDX maps, anhydrous silicate crystals are easily identified as bright, dense objects with clear boundaries.

All five TAM micrometeorites have high phyllosilicate fractions, ranging between 93-98% (TAM15-11: 98%, TAM19B-7: 97%, TAM19B-17: 96%, TAM66-1: 95% and TAM19B-18: 93%). These are plotted in Fig.9, against the existing data, calculated by Howard et al., (2015), from CM, CR and ungrouped C2 chondrites. Using this modal mineralogy metric, the inferred subtypes are at the extreme end-member of the range with petrologic subtypes <1.1. They therefore represent samples from nearly completely hydrated chondrites, closely associated with the C1 class. In addition to intense alteration degrees, the relative alteration sequence of the five samples is similar to the relative sequence determined from the geochemical data; from least to most altered this is: TAM19B-18<TAM66-1<TAM19B-17 <TAM19B-7<TAM15-11.

However, because this study analyses such small particles, these micrometeorites are unlikely to be representative samples of their parent bodies. Consequently, their source asteroid's petrologic subtype is likely to be less-altered than these data suggest. This is because, further analysis of a larger cm-scale fragments is likely to uncover additional coarse-grained anhydrous components. We therefore, suggest that the assigned petrologic subtypes should be viewed as the maximum possible degree of alteration.

5.5. Shock deformation in fine-grained micrometeorites – An increasingly common observation among CM chondrites is the association of higher degrees of aqueous alteration and the presence of impact deformation features, including brecciation and pervasive petrofabrics (Zolensky et al., 1997; Rubin, 2012; Hanna et al., 2015; Lindgren et al., 2015). Foliation within chondrites is discernible through the alignment of phyllosilicates (Rubin et al., 2007; Rubin, 2012), which wrap around chondrules (Hanna et al., 2015), while the presence of subparallel fractures, mineralised veins (Lindgren et al., 2015), cataclasis textures (Hanna et al., 2015) and aligned elongated, elliptical or crushed chondrules (Lindgren et al., 2015) also attest to impact processing. The apparent correlation between pervasive shock fabrics and enhanced aqueous alteration has, therefore, led to the suggestion that impact events provide the necessary heat energy to drives hydrothermal alteration on primitive asteroids (Rubin, 2012; Lindgren et al., 2015).

In contrast, shock deformation in micrometeorites was initially reported by Genge, (2007) and inferred from the presence of shock blackening, metal-sulfide melt veins, similar to those identified in shocked chondrules within olivine grains with numerous subdomains, similar to mosaic extinction patterns that develop at high shock pressures (20-60GPa, Scott et al., 1992) and from the presence of highly vesicular glass, representing shock melting at extreme peak pressures >50GPa (Tomeoka et al., 1999). More recently, low-grade (<5GPa), subtle shock fabrics in small fine-grained Antarctic micrometeorites were revealed through the alignment of dehydration cracks, vesicles and fractures. A preferred orientation was identified in the majority of micrometeorites analysed (80%, Suttle et al., 2017c). These petrofabrics form when aligned phyllosilicates within the matrix of hydrated dust grains are subject to atmospheric entry heating, forming dehydration cracks, and later vesicles. The formation of voids is partially constrained by the orientation of the host phyllosilicates (Nozaki et al., 2006; Suttle et al., 2017c) and, therefore, provides a metric to trace pre-atmospheric anisotropies within the micrometeorite that were present on the parent asteroid (Suttle et al., 2017c).

Our study further supports the link between shock features and aqueous alteration in hydrated carbonaceous chondrites. This is because four of the five micrometeorites studied here are both intensely altered and show evidence of a distinct petrofabric with a uniaxial or pseudo-uniaxial distribution (Fig.10). They share low entropy values, lower than or equivalent to the entropy values obtained from Cold Bokkeveld (S=2.619) and Jbilet Winselwan (S=2.783), which are recognised as regolith breccias with documented shock textures (Metzler et al., 1992; Zolensky et al., 2016). Furthermore, in the case of TAM19B-7 the elongation direction of the elliptical chondrule pseudomorph is also parallel to the elongation direction of the particle's voids strongly suggesting an impact origin to this micrometeorite's petrofabric. However, we do not find a close correlation between each micrometeorite's petrofabric strength (entropy value, S) and their relative degree of aqueous alteration, as determined by either the modal mineralogy or matrix geochemistry metrics. Thus, these two geological processes are not directly related.

6. Implications

6.1. Aqueous alteration among the fine-grained micrometeorite flux – The apparent paucity of recognisable, whole chondrules among Antarctic micrometeorite collections, <<1% among the SPWW collection (Taylor et al., 2012) and <3% within the Larkman Nunatak collection (Genge et al., 2018) has previously been taken as evidence that fine-grained micrometeorites sample a chondrule-poor, matrix-rich parent body, related to, but distinct from, the established hydrated chondrite groups (Engrand and Maurette, 1998; Varela and Kurat, 2009 (and references therein); Reshma et al., 2013). However, the small size (<100µm) of most Antarctic micrometeorites prevents individual grains from sampling whole chondrules (Fig.12 in Genge, 2006), whose diameters typically exceed 250µm (Jones, 2012). Instead, chondrules are represented among micrometeorite collections as fragmented shards and classified as coarse-grained or composite particles (Genge, et al., 2005; 2008; van Ginneken et al., 2017).

Estimates for the abundance of coarse and composite micrometeorites are, at present, poorly constrained but likely represent between 10-30% of the total micrometeorite flux (Kurat et al., 1994; Taylor et al., 2012). However, up to 70% of this material is geochemically related to ordinary chondrite precursors (Genge, 2008), leaving little remaining material to account for the hydrated chondrule budget (perhaps as little as 2% of the total flux). For comparison, most CM and CR chondrites are composed of ~20-50% chondrules by volume (Weisberg, et al., 2006). Thus, it appears that hydrated fine-grained micrometeorites – like those analysed in this study – are moderately-to-severely underrepresented in C2 chondrule material, by potentially up to 1 order of magnitude.

Among the TAM micrometeorite collection, the analysis of significantly larger and, therefore, more representative micrometeorites should result in the identification of CM, CR and C2 ungrouped micrometeorites containing intact chondrules. However, only a single micrometeorite with an unaltered anhydrous CM chondrule (TAM2.1i, Fig.5 in van Ginneken et al., 2012) has so far been identified among a population of >100 TAM micrometeorites. Thus, unaltered and unfragmented chondrules derived from hydrated chondritic parent bodies are extremely rare.

In this study, we investigated five giant fine-grained micrometeorites, representing >2mm^2 of fine-grained matrix. Despite this relatively large area, only 4-5 pseudomorphic chondrules and several small altered CAIs were identified, giving a combined chondrule-to-matrix ratio of just 6.45% ([0.14/2.22]mm^2). We therefore argue that these micrometeorites represent samples of intensely

aqueously altered chondritic matrix, with genetic affinities to the C1 chondrites. Likewise, it seems probable that a significant fraction of micrometeorite flux reaching the Earth today, must also originate from equivalent intensely aqueously altered asteroids. This scenario would then explain a reduced flux of recognisable chondrule material from hydrated carbonaceous parent bodies whilst also supporting the well-documented genetic match between (most) fine-grained micrometeorites and fine-grained CM/CR/C2 matrix.

6.2. The parent bodies of fine-grained micrometeorites – When cosmic dust is released from its parent body, it rapidly (<10Ma) spirals into the inner solar system, losing angular momentum as solar radiation pressure exerts a force tangential to its orbit (Wyatt and Whipple 1950; Gonczi et al., 1982). This delivery mechanism, referred to as Poynting–Robertson (P-R) drag ensures that all mm-scale cosmic dust is ultimately either captured by the terrestrial planets or consumed by the Sun. Consequently, micrometeorites are expected to sample significantly more parent bodies than meteorites and, thus, sample a more diverse population of asteroids. This will necessarily include contributions from both the established carbonaceous chondrite groups as well as otherwise unsampled chondritic parent bodies. We should, therefore, expect micrometeorite collections to contain both particles with direct affinities to CM, CR and CI chondrites as well as micrometeorites whose petrographic affinities are inconsistent with established groups.

However, we also propose that some of the observed petrographic differences between fine-grained micrometeorites and CM/CR/CI chondrites are explainable as a result of sampling biases. Because the petrographic properties of established carbonaceous chondrite groups are defined only from meteorites, and since meteorites are known to originate from a limited number of parent bodies (~110, Greenwood et al., 2016), it is probable that the full range of petrographic properties for each chondrite group (CR, CM, CI etc.) are not accurately sampled. Likewise, it is also possible that many of the fine-grained micrometeorites originate from the same parent bodies as meteorites but are not recognised as such because they have geochemical, organic matter or isotopic signatures which fall outside the defined range. Thus, we suggest that some of the differences between fine-grained micrometeorites and CM/CR/CI chondrites are a product of sampling issues.

7. Conclusions

This study investigated five giant fine-grained micrometeorites whose petrographies are dominated by hydrated secondary minerals formed during advanced aqueous alteration. They contain multiple generations of phyllosilicate growth, evidenced by cross-cutting relationships, variable cation compositions and a range of grain sizes. Meanwhile, unaltered coarse-grained, structural components such as chondrules, CAIs and AOAs are either rare or entirely absent, having been replaced by indistinct chondrule pseudomorphs and partially consumed CAIs. These micrometeorites, therefore, share many similarities with the intensely altered CM1, CR1 and CI carbonaceous chondrites. Four of the five micrometeorites also show evidence of pervasive uniaxial petrofabrics, most likely generated by impact processing. This is most evident in TAM19B-7, in which the alignment of matrix phyllosilicates is parallel to the elongation direction of a compacted chondrule pseudomorph.

On the basis of our findings and previous studies researching small fine-grained micrometeorites we propose that much of the fine-grained dust flux is most likely derived from established hydrated carbonaceous chondrites groups and that their intensely altered compositions suggest the C-type asteroid population contains many hydrated bodies with high water contents.

8. Acknowledgements

The data presented in this paper were acquired during Martin Suttle's PhD research whilst at Imperial College London and the NHM - funded by the Science and Technology Council (STFC) (ST/M503526/1). Research continued whilst I attended a post-doc research position at the University of Pisa, which is funded through two Italian research grants MIUR: PNRA16_00029 [Programma Nazionale delle Ricerche in Antartide – CUP I52F17001050005] and PRIN2015_20158W4JZ7 [CUP I52F15000310001 for the "Meteoriti Antartiche"]. L. Folco is also supported through the same research grants, while Matthew Genge and Sara Russell are funded by the STFC grants (ST/J001260/1 and ST/M00094X/1 respectively). We thank John Spratt, Tomasz Góral and Tobias Salge at the NHM, London for their support and advice during and analytical acquisition. Further, we thank two anonymous reviewers and Kieran Howard for their suggestions and comments during the review process as well as the work of associate editor Eric Quirico and Executive editor Marc Norman for their handling of this manuscript.

9. References

Alexander, C.M.D., Taylor, S., Delaney, J.S., Ma, P. and Herzog, G.F., 2002. Mass-dependent fractionation of Mg, Si, and Fe isotopes in five stony cosmic spherules. *Geochim. Cosmochim. Acta* **66**, 173-183, doi:10.1016/S0016-7037(01)00764-5.

Battandier, M., Bonal, L., Quirico, E., Beck, P., Engrand, C., Duprat, J. and Dartois, E., 2018. Characterization of the organic matter and hydration state of Antarctic micrometeorites: A reservoir distinct from carbonaceous chondrites. *Icarus* **306**, 74-93, doi:10.1016/j.icarus.2018.02.002.

Beck, P., Maturilli, A., Garenne, A., Vernazza, P., Helbert, J., Quirico, E. and Schmitt, B., 2018. What is controlling the reflectance spectra (0.35–150 µm) of hydrated (and dehydrated) carbonaceous chondrites?. *Icarus* **313**, 124-138, doi:10.1016/j.icarus.2018.05.010.

Bland, P.A., Kelley, S.P., Berry, F.J., Cadogan, J.M. and Pillinger, C.T., 1997. Artificial weathering of the ordinary chondrite Allegan: Implications for the presence of Cl–as a structural component in akaganeite. *American Mineralogist* **82**, 1187-1197, doi:10.2138/am-1997-11-1215.

Bland, P.A., Cressey, G. and Menzies, O.N., 2004. Modal mineralogy of carbonaceous chondrites by X-ray diffraction and Mössbauer spectroscopy. *Meteoritics Planet.Sci.* **39**, 3-16, doi:10.1111/j.1945-5100.2004.tb00046.x.

Bland, P.A., Jackson, M.D., Coker, R.F., Cohen, B.A., Webber, J.B.W., Lee, M.R., Duffy, C.M., Chater, R.J., Ardakani, M.G., McPhail, D.S. and McComb, D.W., 2009. Why aqueous alteration in asteroids was isochemical: High porosity≠ high permeability. *Earth Planet. Sci. Lett.*, **287**, 559-568, doi:10.1016/j.epsl.2009.09.004.

Browning, L.B., McSween Jr, H.Y. and Zolensky, M.E., 1996. Correlated alteration effects in CM carbonaceous chondrites. *Geochim. Cosmochim. Acta* **60**, 2621-2633, doi:10.1016/0016-7037(96)00121-4.

Ciesla, F.J., Lauretta, D.S., Cohen, B.A. and Hood, L.L., 2003. A nebular origin for chondritic fine-grained phyllosilicates. *Science*, **299**, 549-552, doi:10.1126/science.1079427.

Doyle, P.M., Jogo, K., Nagashima, K., Krot, A.N., Wakita, S., Ciesla, F.J. and Hutcheon, I.D., 2015. Early aqueous activity on the ordinary and carbonaceous chondrite parent bodies recorded by fayalite. *Nature communications*, **6**, 7444, doi:10.1038/ncomms8444.

Elmaleh, A., Bourdelle, F., Caste, F., Benzerara, K., Leroux, H. and Devouard, B., 2015. Formation and transformations of Fe-rich serpentines by asteroidal aqueous alteration processes: A nanoscale study of the Murray chondrite. *Geochim. Cosmochim. Acta* **158**, 162-178, doi:10.1016/j.gca.2015.03.007.

Engrand, C. and Maurette, M., 1998. Carbonaceous micrometeorites from Antarctica. *Meteoritics Planet. Sci.* **33**, 565-580, doi:10.1111/j.1945-5100.1998.tb01665.x.

759 Folco, L., Rochette, P., Perchiazzi, N., d'Orazio, M., Laurenzi, M.A. and Tiepolo, M., 2008. Microtektites from
760 Victoria Land Transantarctic Mountains. *Geology*, **36**, 291-294, doi:10.1130/G24528A.

761 Friend, P., Hezel, D.C., Barrat, J.A., Zipfel, J., Palme, H. and Metzler, K., 2018. Composition, petrology, and
762 chondrule-matrix complementarity of the recently discovered Jbilet Winselwan CM2 chondrite. *Meteoritics*
763 *Planet.Sci*, doi:10.1111/maps.13139.

764 Genge, M.J., 2002. Hydrated Chondrule Fragments Amongst Micrometeorites. 65th *Annual Meeting of the*
765 *Meteoritical Society*, held July 21-26, 2002 in Los Angeles, California. (abstract #5102).

766 Genge, M.J., 2006. Igneous rims on micrometeorites. *Geochim. Cosmochim. Acta* **70**, 2603-2621,
767 doi:10.1016/j.gca.2006.02.005.

768 Genge, M.J., 2007. Evidence for Shock in Micrometeorites: *70th Annual Meeting of the Meteoritical Society, held*
769 *August 13-17, Tucson, Arizona.* (abstract #5007).

770 Genge, M.J., 2008. Koronis asteroid dust within Antarctic ice. *Geology* **36**, 687-690, doi:10.1130/G24493A.1.

771 Genge, M.J., Gileski, A. and Grady, M.M., 2005. Chondrules in Antarctic micrometeorites *Meteoritics Planet.Sci.*
772 **40**, 225-238, doi:10.1111/j.1945-5100.2005.tb00377.x.

773 Genge, M.J., Engrand, C., Gounelle, M. and Taylor, S., 2008. The classification of micrometeorites. *Meteoritics*
774 *Planet.Sci.* **43**, 497-515, doi:10.1111/j.1945-5100.2008.tb00668.x.

775 Genge, M.J., van Ginneken, M., Suttle, M.D. and Harvey, R.P., 2018. Accumulation mechanisms of
776 micrometeorites in an ancient supraglacial moraine at Larkman Nunatak, Antarctica. *Meteoritics Planet. Sci.*
777 doi:10.1111/maps.13107

778 Gonczi, R., Froeschlé, C. and Froeschlé, C., 1982. Poynting-Robertson drag and orbital resonance. *Icarus* **51**, 633-
779 654, doi:10.1016/0019-1035(82)90152-X.

780 Greenwood, R.C., Lee, M.R., Hutchison, R. and Barber, D.J., 1994. Formation and alteration of CAIs in Cold
781 Bokkeveld (CM2). *Geochim. Cosmochim. Acta* **58**, 1913-1935, doi:10.1016/0016-7037(94)90424-3.

782 Greenwood, R.C., Burbine, T.H., Miller, M.F. and Franchi, I.A., 2017. Melting and differentiation of early-formed
783 asteroids: The perspective from high precision oxygen isotope studies. *Chemie der Erde* **77**, 1-43,
784 doi:10.1016/j.chemer.2016.09.005.

785 Hanna, R.D., Ketcham, R.A., Zolensky, M. and Behr, W.M., 2015. Impact-induced brittle deformation, porosity
786 loss, and aqueous alteration in the Murchison CM chondrite. *Geochim. Cosmochim. Acta* **171**, 256-282,
787 doi:10.1016/j.gca.2015.09.005.

788 Harju, E.R., Rubin, A.E., Ahn, I., Choi, B.G., Ziegler, K. and Wasson, J.T., 2014. Progressive aqueous alteration of
789 CR carbonaceous chondrites. *Geochim. Cosmochim. Acta* **58**, 267-292, doi:10.1016/j.gca.2014.04.048.

790 Hewins, R.H., Bourot-Denise, M., Zanda, B., Leroux, H., Barrat, J.A., Humayun, M., Göpel, C., Greenwood, R.C.,
791 Franchi, I.A., Pont, S. and Lorand, J.P., 2014. The Paris meteorite, the least altered CM chondrite so far. *Geochim.*
792 *Cosmochim. Acta* **124**, 190-222, doi:10.1016/j.gca.2013.09.014.

793 Hezel, D.C., Russell, S.S., Ross, A.J. and Kearsley, A.T., 2008. Modal abundances of CAIs: Implications for bulk
794 chondrite element abundances and fractionations. *Meteoritics Planet.Sci.* **43**, 1879-1894, doi:10.1111/j.1945-
795 5100.2008.tb00649.x.

796 Howard, K.T., Benedix, G.K., Bland, P.A. and Cressey, G., 2009. Modal mineralogy of CM2 chondrites by X-ray
797 diffraction (PSD-XRD). Part 1: Total phyllosilicate abundance and the degree of aqueous alteration. *Geochim.*
798 *Cosmochim. Acta* ***73***, 4576-4589, doi:10.1016/j.gca.2009.04.038.

799 Howard, K.T., Alexander, C.O.D., Schrader, D.L. and Dyl, K.A., 2015. Classification of hydrous meteorites (CR, CM
800 and C2 ungrouped) by phyllosilicate fraction: PSD-XRD modal mineralogy and planetesimal environments.
801 *Geochim. Cosmochim. Acta* **149**, 206-222, doi:.10.1016/j.gca.2014.10.025

802 Jones, R.H., 2012. Petrographic constraints on the diversity of chondrule reservoirs in the protoplanetary disk.
803 *Meteoritics Planet.Sci.* **47**, 1176-1190, doi:10.1111/j.1945-5100.2011.01327.x.

804 King, A.J., Schofield, P.F., Howard, K.T. and Russell, S.S., 2015. Modal mineralogy of CI and CI-like chondrites by
805 X-ray diffraction. *Geochim. Cosmochim. Acta* **165**, 148-160, doi:10.1016/j.gca.2015.05.038.

806 King, A.J., Schofield, P.F. and Russell, S.S., 2017. Type 1 aqueous alteration in CM carbonaceous chondrites:
807 Implications for the evolution of water-rich asteroids. *Meteoritics Planet. Sci.* **52**, 1197-1215,
808 doi:10.1111/maps.12872Krot, A.N., Petaev, M.I. and Yurimoto, H., 2004. Amoeboid olivine aggregates with low-
809 Ca pyroxenes: a genetic link between refractory inclusions and chondrules?. *Geochim. Cosmochim. Acta* **68**,
810 1923-1941, doi:10.1016/j.gca.2003.10.026.

811 Kurat, G., Brandstaetter, F., Maurette, M. and Coeberl, C., 1991. CI-like micrometeorites from Cap Prudhomme,
812 Antarctica. *Lunar Planet. Sci. XXIII.* Lunar Planet. Inst., Houston. #747(abstr.)

813 Kurat, G., Koeberl, C., Presper, T., Brandstätter, F. and Maurette, M., 1994. Petrology and geochemistry of
814 Antarctic micrometeorites. *Geochim. Cosmochim. Acta* **58***,* 3879-3904, doi:10.1016/0016-7037(94)90369-7.

815 Le Guillou, C., Changela, H.G. and Brearley, A.J., 2015. Widespread oxidized and hydrated amorphous silicates in
816 CR chondrites matrices: Implications for alteration conditions and H2 degassing of asteroids. *Earth and Planet.*
817 *Sci. Lett.*, **420**, 162-173, doi:10.1016/j.epsl.2015.02.031.

818 Lee, M.R., Lindgren, P., Sofe, M.R., Alexander, C.O.D. and Wang, J., 2012. Extended chronologies of aqueous
819 alteration in the CM2 carbonaceous chondrites: Evidence from carbonates in Queen Alexandra Range
820 93005. *Geochim. Cosmochim. Acta* **92**, 148-169, doi:10.1016/j.gca.2012.06.005.

821 Lee, M.R., Sofe, M.R., Lindgren, P., Starkey, N.A. and Franchi, I.A., 2013. The oxygen isotope evolution of parent
822 body aqueous solutions as recorded by multiple carbonate generations in the Lonewolf Nunataks 94101 CM2
823 carbonaceous chondrite. *Geochim. Cosmochim. Acta* **121**, 452-466, doi:10.1016/j.gca.2013.07.010.

824 Lee, M.R., Lindgren, P. and Sofe, M.R., 2014. Aragonite, breunnerite, calcite and dolomite in the CM
825 carbonaceous chondrites: High fidelity recorders of progressive parent body aqueous alteration. *Geochim.*
826 *Cosmochim. Acta* **144**, 126-156, doi:10.1016/j.gca.2014.08.019.

827 Lee, M.R. and Lindgren, P., 2016. Aqueous alteration of chondrules from the Murchison CM carbonaceous
828 chondrite: Replacement, pore filling, and the genesis of polyhedral serpentine. *Meteoritics Planet. Sci.* **51**, 1003-
829 1021, doi:10.1111/maps.12644.

830 Leroux, H., Cuvillier, P., Zanda, B. and Hewins, R.H., 2015. GEMS-like material in the matrix of the Paris meteorite
831 and the early stages of alteration of CM chondrites. *Geochim. Cosmochim. Acta* **170**, 247-265,
832 doi:10.1016/j.gca.2015.09.019.

833 Lindgren, P., Hanna, R.D., Dobson, K.J., Tomkinson, T. and Lee, M.R., 2015. The paradox between low shock-
834 stage and evidence for compaction in CM carbonaceous chondrites explained by multiple low-intensity impacts.
835 *Geochim. Cosmochim. Acta* **148**, 159-178, doi: 10.1016/j.gca.2014.09.014.

836 Lodders, K., 2003. Solar system abundances and condensation temperatures of the elements. *The Astrophys.*
837 *Journ.* **591**, 1220-1247, doi:10.1086/375492.

838 Maharaj, S.V. and Hewins, R.H., 1994. Clues to chondrule precursors: An investigation of vesicle formation in
839 experimental chondrules. *Geochim. Cosmochim. Acta* **58**, 1335-1342, doi:10.1016/0016-7037(94)90385-9.

840 Marrocchi, Y., Gounelle, M., Blanchard, I., Caste, F. and Kearsley, A.T., 2014. The Paris CM chondrite: Secondary
841 minerals and asteroidal processing. *Meteoritics Planet. Sci.* **49**, 1232-1249, doi:10.1111/maps.12329.

842 McSween Jr, H.Y., 1979. Alteration in CM carbonaceous chondrites inferred from modal and chemical variations
843 in matrix. *Geochim. Cosmochim. Acta* **43**, 1761-1770, doi:10.1016/0016-7037(79)90024-3.

844 McSween Jr, H.Y., 1987. Aqueous alteration in carbonaceous chondrites: Mass balance constraints on matrix
845 mineralogy. *Geochim. Cosmochim. Acta* **51**, 2469-2477, doi:10.1016/0016-7037(87)90298-5.

Metzler, K., Bischoff, A., and Stöffler, D. 1992. Accretionary dust mantles in CM chondrites: Evidence for solar nebula processes. *Geochim. Cosmochim. Acta* **56**, 2873-2897, doi:10.1016/0016-7037(92)90365-P.

Nakamura, T., 2005. Post-hydration thermal metamorphism of carbonaceous chondrites. *Journ. Mineralog. Petrolog. Sci.* **100**, 260-272, doi:10.2465/jmps.100.260.

Noguchi, T., Yabuta, H., Itoh, S., Sakamoto, N., Mitsunari, T., Okubo, A., Okazaki, R., Nakamura, T., Tachibana, S., Terada, K. and Ebihara, M., 2017. Variation of mineralogy and organic material during the early stages of aqueous activity recorded in Antarctic micrometeorites. *Geochim. Cosmochim. Acta* **208**, 119-144, doi:10.1016/j.gca.2017.03.034.

Nozaki, W., Nakamura, T. and Noguchi, T., 2006. Bulk mineralogical changes of hydrous micrometeorites during heating in the upper atmosphere at temperatures below 1000C. *Meteoritics Planet. Sci.* **41,** 1095-1114, doi:10.1111/j.1945-5100.2006.tb00507.x.

Pernet-Fisher, J.F., Howarth, G.H., Barry, P.H., Bodnar, R.J. and Taylor, L.A., 2014, March. The extent of aqueous alteration within the Jbilet Winselwan CM2 chondrite. *Lunar Planet. Sci. XXXXV Lunar Planet. Inst., Houston. #2386(abstr.)*.

Pignatelli, I., Marrocchi, Y., Vacher, L.G., Delon, R. and Gounelle, M., 2016. Multiple precursors of secondary mineralogical assemblages in CM chondrites. *Meteoritics Planet. Sci.* **51,** 785-805, doi:10.1111/maps.12625.

Reshma, K., Rudraswami, N.G. and Prasad, M.S., 2013. Chondrule-like object from the Indian Ocean cosmic spherules*. Journ. Earth System Sci.* **122**, 1161-1171, doi:10.1007/s12040-013-0333-8.

Rietmeijer, F.J., 1991. Aqueous alteration in five chondritic porous interplanetary dust particles. *Earth Planet. Sci. Lett.* **102**, 48-157, doi:10.1016/0012-821X(91)90004-2.

Rubin, A.E., 2012. Collisional facilitation of aqueous alteration of CM and CV carbonaceous chondrites. *Geochim. Cosmochim. Acta* **90**, 181-194, doi:10.1016/j.gca.2012.05.016.

Rubin, A.E. and Wasson, J.T., 1986. Chondrules in the Murray CM2 meteorite and compositional differences between CM-CO and ordinary chondrite chondrules. *Geochim. Cosmochim. Acta* **50**, 307-315, doi:10.1016/0016-7037(86)90179-1.

Rubin, A.E., Trigo-Rodríguez, J.M., Huber, H. and Wasson, J.T., 2007. Progressive aqueous alteration of CM carbonaceous chondrites. *Geochim. Cosmochim. Acta* **71**, 2361-2382, doi:10.1016/j.gca.2007.02.008.

Scott, E.R., Keil, K. and Stoeffler, D., 1992. Shock metamorphism of carbonaceous chondrites. *Geochim. Cosmochim. Acta* **56**, 4281-4293, doi:10.1016/0016-7037(92)90268-N.

Steele, I.M., 1992. Olivine in Antarctic micrometeorites: Comparison with other extraterrestrial olivine. . *Geochim. Cosmochim. Acta* **56**, 2923-2929, doi:10.1016/0016-7037(92)90368-S.

Suavet, C., Rochette, P., Kars, M., Gattacceca, J., Folco, L. and Harvey, R.P., 2009. Statistical properties of the Transantarctic Mountains (TAM) micrometeorite collection. *Polar Sci.* **3**, 100-109, doi:10.1016/j.polar.2009.06.003.

Suavet, C., Alexandre, A., Franchi, I.A., Gattacceca, J., Sonzogni, C., Greenwood, R.C., Folco, L. and Rochette, P., 2010. Identification of the parent bodies of micrometeorites with high-precision oxygen isotope ratios. *Earth Planet. Sci. Lett.* **293**, 313-320, doi:10.1016/j.epsl.2010.02.046.

Suavet, C., Gattacceca, J., Rochette, P. and Folco, L., 2011. Constraining the terrestrial age of micrometeorites using their record of the Earth's magnetic field polarity. *Geology* **39**, 123-126, doi:10.1130/G31655.1.

Suttle, M.D., Genge, M.J., Folco, L. and Russell, S.S., 2017a. The thermal decomposition of fine-grained micrometeorites, observations from mid-IR spectroscopy. *Geochim. Cosmochim. Acta* **206**, 112-136, doi:10.1016/j.gca.2017.03.002.

Suttle, M.D. and Genge, M.J., 2017b. Diagenetically altered fossil micrometeorites suggest cosmic dust is common the geological record. *Earth Planet. Sci. Lett.* **476**, 132-142, doi:10.1016/j.epsl.2017.07.052.

Suttle, M.D., Genge, M.J., Russell, S.S., 2017c. Shock fabrics in fine-grained micrometeorites. *Meteoritics Planet. Sci.* doi:10.1111/maps.12927.

Suttle, M.D., Genge, M.J., Folco, L., Lin, Q., Russell, S.S., and Najorka, J. 2018. The atmospheric entry of fine-grained micrometeorites: the role of volatile gases in heating and fragmentation. *Meteoritics Planet. Sci.* doi:10.1111/MAPS.13220-2921

Takayama, A. and Tomeoka, K., 2012. Fine-grained rims surrounding chondrules in the Tagish Lake carbonaceous chondrite: Verification of their formation through parent-body processes. *Geochim. Cosmochim. Acta* **98**, 1-18, doi:10.1016/j.gca.2012.08.015.

Takir, D., Emery, J.P., Mcsween, H.Y., Hibbitts, C.A., Clark, R.N., Pearson, N. and Wang, A., 2013. Nature and degree of aqueous alteration in CM and CI carbonaceous chondrites. *Meteoritics Planet. Sci. **48**,* 1618-1637, doi:10.1111/maps.12171.

Taylor, S., Matrajt, G. and Guan, Y., 2012. Fine-grained precursors dominate the micrometeorite flux. *Meteoritics Planet. Sci.* **47**, 550-564, doi:10.1111/j.1945-5100.2011.01292.

Tomeoka, K. and Buseck, P.R., 1985. Indicators of aqueous alteration in CM carbonaceous chondrites: Microtextures of a layered mineral containing Fe, S, O and Ni. *Geochim. Cosmochim. Acta* **49**, 2149-2163, doi:10.1016/0016-7037(85)90073-0.

Tonui, E.K., Zolensky, M.E., Lipschutz, M.E., Wang, M.S. and Nakamura, T., 2003. Yamato 86029: Aqueously altered and thermally metamorphosed CI-like chondrite with unusual textures. *Meteoritics Planet. Sci.* **38**, 69-292, doi:10.1111/j.1945-5100.2003.tb00264.x.

Toppani, A., Libourel, G., Engrand, C. and Maurette, M., 2001. Experimental simulation of atmospheric entry of micrometeorites. *Meteoritics Planet. Sci.* **36**, 1377-1396, doi:10.1111/j.1945-5100.2001.tb01831.x.

Trigo-Rodriguez, J.M., Rubin, A.E. and Wasson, J.T., 2006. Non-nebular origin of dark mantles around chondrules and inclusions in CM chondrites. *Geochim. Cosmochim. Acta* **70**, 1271-1290, doi:10.1016/j.gca.2005.11.009.

van Ginneken, M., Folco, L., Cordier, C. and Rochette, P., 2012. Chondritic micrometeorites from the Transantarctic Mountains. *Meteoritics Planet. Sci.* **47**, 228-247, doi: 10.1111/j.1945-5100.2011.01322.x

van Ginneken, M., Genge, M.J., Folco, L. and Harvey, R.P., 2016. The weathering of micrometeorites from the Transantarctic Mountains. *Geochim. Cosmochim. Acta* **179**, 1-31, doi: 10.1016/j.gca.2015.11.045.

van Ginneken, M., Gattacceca, J., Rochette, P., Sonzogni, C., Alexandre, A., Vidal, V. and Genge, M.J., 2017. The parent body controls on cosmic spherule texture: Evidence from the oxygen isotopic compositions of large micrometeorites. *Geochim. Cosmochim. Acta*, doi:10.1016/j.gca.2017.05.008

Varela, M.E. and Kurat, G., 2009. Glasses in coarse-grained micrometeorites. *Earth Planet. Sci. Lett*. **284**, 208-218, doi:10.1016/j.epsl.2009.04.030.

Velbel, M.A., Tonui, E.K. and Zolensky, M.E., 2012. Replacement of olivine by serpentine in the carbonaceous chondrite Nogoya (CM2). *Geochim. Cosmochim. Acta* **87**, 117-135, doi:10.1016/j.gca.2012.03.016.

Wasson, J.T. and Rubin, A.E., 2014. Absence of matrix-like chondrule rims in CR2 LAP 02342. *Meteoritics Planet. Sci.* **49**, 245-260, doi:10.1111/maps.12237.

Weisberg, M.K., McCoy, T.J. and Krot, A.N., 2006. Systematics and evaluation of meteorite classification. In *Meteorites and the Early Solar System II*, D. S. Lauretta and H. Y. McSween Jr. (eds.), University of Arizona Press, Tucson, 943:19-52.

Weisberg, M.K. and Huber, H., 2007. The GRO 95577 CR1 chondrite and hydration of the CR parent body. *Meteoritics Planet. Sci.* **42**, 1495-1503, doi:10.1111/j.1945-5100.2007.tb00587.x

Welten, K.C., Folco, L., Nishiizumi, K., Caffee, M.W., Grimberg, A., Meier, M.M.M. and Kober, F., 2008. Meteoritic and bedrock constraints on the glacial history of Frontier Mountain in northern Victoria Land, Antarctica. *Earth Planet. Sci. Lett.* **270**, 308-315, doi:10.1016/j.epsl.2008.03.052.

Wyatt, S.P. and Whipple, F.L., 1950. The Poynting-Robertson effect on meteor orbits. *The Astrophys. Journ.* **111**, 134-141.

Zolensky, M.E., Ivanov, A.V., Yang, S.V., Mittlefehldt, D.W. and Ohsumi, K., 1996. The Kaidun meteorite: Mineralogy of an unusual CM1 lithology. *Meteoritics Planet. Sci.* **31**, 484-493, doi:10.1111/j.1945-5100.1996.tb02090.x.

Zolensky, M.E., Mittlefehldt, D.W., Lipschutz, M.E., Wang, M.S., Clayton, R.N., Mayeda, T.K., Grady, M.M., Pillinger, C. and David, B., 1997. CM chondrites exhibit the complete petrologic range from type 2 to 1: *Geochim. Cosmochim. Acta* **61**, 5099-5115, doi:10.1016/S0016-7037(97)00357-8.

Zolensky, M.E., Zega, T.J., Yano, H., Wirick, S., Westphal, A.J., Weisberg, M.K., Weber, I., Warren, J.L., Velbel, M.A., Tsuchiyama, A. and Tsou, P., 2006. Mineralogy and petrology of comet 81P/Wild 2 nucleus samples. *Science*, **314**, 1735-1739, doi:10.1126/science.1135842.

Zolensky, M., Mikouchi, T., Fries, M., Bodnar, R., Jenniskens, P., Yin, Q.Z., Hagiya, K., Ohsumi, K., Komatsu, M., Colbert, M. and Hanna, R., 2014. Mineralogy and petrography of C asteroid regolith: The Sutter's Mill CM meteorite. *Meteoritics Planet. Sci.* **49**, 1997-2016, doi:10.1111/maps.12386.

Zolensky, M., Mikouchi, T., Hagiya, K., Ohsumi, K., Komatsu, M., Chan, Q.H., Le, L., Kring, D., Cato, M., Fagan, A.L. and Gross, J., 2016b. Unique View of C Asteroid Regolith from the Jbilet Winselwan CM Chondrite (abstract #2148) 46th Lunar and Planetary Science Conference. CD-ROM

List of Tables and Figures:

Fig.1. SEM-BEI data and element maps for TAM19B-7
Fig.2. SEM-BEI data and element maps for TAM19B-17
Fig.3. SEM-BEI data and elemental maps for TAM19B-18
Fig.4. SEM-BEI data for TAM15-11
Fig.5. SEM-BEI data and elemental maps for TAM66-1
Fig.6. Micrometeorite matrix geochemistry: spider diagram elemental abundance normalized to CI concentrations.
Fig.7. Micro-XRD patterns for three of the giant micrometeorites
Fig.8. Matrix geochemistry and inferred degree of alteration.
Fig.9. Estimated phyllosilicate fraction and inferred petrologic subtype, modified after Howard et al., (2015).
Fig.10. 2D petrofabric analyses for the five micrometeorites

Table.1. Analysis types collected on each micrometeorite.
Table.2. Geochemical data (WD-EMPA and standard-based SEM-EDS spot analyses) collected from the particle matrix, anhydrous silicates, sulfides, CAIs and terrestrial alteration rims.
Table.3. Petrofabric analysis, circular statistics and entropy data.
Table.S1. Supplementary data file, uploaded as an excel file [not shown here] containing the bulk matrix geochemistry of 77 small, fine-grained Antarctic micrometeorites from the Cap Prud'homme collection. Data was used in Fig.9.

974 # Tables

975 **Table.1**. Analysis types performed on each micrometeorite

Micrometeorite	Exposed surface area (mm^2)	BEI Exterior	BEI Interior	WD-EMPA [Cameca]	Standard-based EDS [Zeiss EVO]	Standard-less EDS [FEI Quanta 450]	EDX map [FEI Quanta 650/450]	µXRD	Fabric analysis	Phyllosilicate fraction
TAM19B-7	1.15		•	•	•	•	•	•	•	•
TAM19B-17	0.21		•	•			•	•	•	•
TAM19B-18	0.27		•	•	•		•	•	•	•
TAM15-11	0.30		•	•		•	•		•	•
TAM66-1	0.29	•	•	•		•	•		•	•

976

977

978

979

980

981

982 **Table.2**. (overleaf) Geochemical data from the five giant TAM micrometeorites. Data includes bulk matrix compositions, typical individual matrix analyses, analyses of
983 altered CAIs, and anhydrous silicates. Data is shown in normalised wt%, although the uncorrected weight totals are also included for reference. Values quoted to 2 decimal
984 places represent analyses collected on the WD-EMPA system, while analyses quotes to 1 decimal place represent data collected on an EDS system (black for standard-
985 based and grey for standard-less). Elements with "*b.d.l*" indicate values which are below detection limits. The location and suspected phase are included in the table and
986 location data can be referenced against the spot locations shown in Figs.1-5.

No.	Particle	Analysis	N=	Al	Ca	Ti	Si	Mg	Fe	Ni	Cr	P	K	Na	S	O	Total	Total	FeO/SiO_2	Mg# [At%]	Location
1	TAM19B-7	**A0**	**51**	**2.8**	**0.1**	***b.d.l***	**22.0**	**2.3**	**26.6**	**0.5**	**0.7**	**0.2**	**1.0**	**0.6**	**3.1**	**40.2**	**100.0**	**83.5**	**0.74**	**18**	**Bulk**
2	TAM19B-7	A1	1	3.4	*b.d.l*	*b.d.l*	19.0	4.4	28.7	*b.d.l*	0.6	*b.d.l*	0.5	0.0	3.5	40.0	100.0	73.0	0.91	26	Matrix analyses
3	TAM19B-7	A2	1	2.4	0.3	*b.d.l*	24.2	5.3	16.7	*b.d.l*	1.1	*b.d.l*	0.5	0.6	1.8	47.2	100.0	94.4	0.42	42	
4	TAM19B-7	A3	1	2.0	0.2	*b.d.l*	22.8	0.6	26.4	*b.d.l*	0.9	0.4	0.3	0.4	1.9	44.1	100.0	84.1	0.70	5	
5	TAM19B-7	A4	1	1.6	*b.d.l*	*b.d.l*	16.3	*b.d.l*	31.9	0.8	0.5	0.2	0.2	0.3	4.1	44.2	100.0	88.4	1.18	-	Fine-grained rim
6	TAM19B-17	**B0**	**25**	**1.88**	**0.15**	**0.10**	**19.63**	**3.40**	**29.82**	**0.16**	**0.43**	**0.18**	**0.68**	**0.20**	**3.04**	**40.21**	**100.00**	**89.45**	**0.98**	**18**	**Bulk**
7	TAM19B-17	B1	1	1.64	0.04	0.08	14.32	4.02	38.57	0.11	0.48	0.21	0.27	0.16	3.10	36.86	100.00	92.51	1.62	19	Matrix analyses
8	TAM19B-17	B2	1	1.87	0.20	0.11	26.87	0.72	23.57	0.07	0.48	0.24	0.59	0.22	1.83	43.17	100.00	81.94	0.53	7	
9	TAM19B-17	B3	1	2.26	0.06	0.06	15.96	7.89	33.39	0.11	0.23	0.03	0.06	0.12	1.72	37.90	100.00	98.58	1.26	35	
10	TAM19B-17	B4	1	3.7	6.8	0.2	20.7	6.0	16.8	*b.d.l*	0.5	0.1	0.6	0.6	1.9	42.0	100.0	101.8	0.5	45	Altered CAI core
11	TAM19B-17	B5	1	5.1	0.3	0.1	16.1	7.1	29.5	0.1	*b.d.l*	0.1	0.3	0.6	1.5	39.0	100.0	87.6	1.1	36	Altered CAI edge
12	TAM19B-17	B6	1	1.8	7.9	*b.d.l*	26.9	10.8	5.7	*b.d.l*	0.4	*b.d.l*	*b.d.l*	*b.d.l*	0.8	45.6	100.0	104.7	0.1	81	Altered CAI other
13	TAM19B-18	**C0**	**17**	**1.76**	**0.16**	**0.06**	**14.82**	**7.76**	**34.75**	**0.26**	**0.31**	**0.08**	**0.34**	**0.22**	**2.05**	**37.21**	**100.00**	**95.83**	**1.35**	**34**	**Bulk**
14	TAM19B-18	C1	1	1.44	0.19	0.07	16.33	10.20	29.92	0.66	0.29	0.07	0.15	0.40	1.62	38.38	100.00	98.55	1.10	44	Matrix analyses
15	TAM19B-18	C2	1	1.57	0.10	0.05	14.90	7.77	36.30	0.12	0.31	0.02	0.14	0.13	1.62	36.72	100.00	96.94	1.47	33	
16	TAM19B-18	C3	1	1.77	0.36	0.06	16.03	6.63	33.99	0.27	0.29	0.05	0.08	0.13	2.24	37.89	100.00	98.94	1.28	31	
17	TAM19B-18	C4	3	1.59	0.24	0.08	18.67	9.11	26.10	0.39	0.50	0.14	0.22	0.36	2.11	40.23	100.00	95.29	0.84	44	Clast
18	TAM19B-18	C5	1	2.5	0.1	*b.d.l*	23.7	2.7	22.1	0.2	0.4	*b.d.l*	0.3	*b.d.l*	3.7	43.4	100.0	80.7	0.56	22	Forsterite
19	TAM19B-18	C6	1	0.3	0.3	*b.d.l*	27.4	23.3	1.0	*b.d.l*	0.3	*b.d.l*	*b.d.l*	*b.d.l*	*b.d.l*	47.3	100.0	100.1	0.02	98	Forsterite
20	TAM15-11	**D0**	**16**	**1.91**	**0.30**	**0.12**	**23.17**	**2.53**	**24.96**	**0.13**	**0.58**	**0.14**	**1.12**	**0.42**	**2.61**	**41.92**	**100.00**	**77.63**	**0.71**	**18**	**Bulk**
21	TAM15-11	D1	1	2.41	0.19	0.12	34.24	2.15	11.11	0.04	0.59	0.04	0.48	0.29	0.73	47.56	100.00	73.07	0.20	31	Matrix analyses
22	TAM15-11	D2	1	2.48	0.17	0.13	29.22	2.77	18.03	0.19	0.66	0.17	0.43	0.37	0.74	44.56	100.00	87.41	0.37	26	
23	TAM15-11	D3	1	1.79	0.18	0.12	20.54	0.84	26.24	0.14	0.51	0.12	3.43	0.47	4.39	41.11	100.00	77.01	0.77	7	
24	TAM15-11	D4	1	20.43	0.13	0.02	3.13	0.17	23.33	0.05	0.21	0.10	4.41	0.07	7.24	40.63	100.00	86.02	4.49	2	Al-Fe Spinel
25	TAM15-11	D5	1	0.5	0.5	*b.d.l*	30.7	20.6	1.7	*b.d.l*	0.4	*b.d.l*	*b.d.l*	*b.d.l*	0.1	45.5	100.0	84.7	0.03	97	Low-Ca Px [En]
26	TAM15-11	D6	1	0.8	15.1	0.6	26.3	12.2	1.0	0.1	0.4	*b.d.l*	*b.d.l*	*b.d.l*	*b.d.l*	43.3	100.0	90.1	0.02	97	High-Ca Px [Aug]
27	TAM15-11	D7	1	1.9	15.0	0.4	25.3	10.0	2.4	*b.d.l*	1.5	*b.d.l*	*b.d.l*	*b.d.l*	*b.d.l*	42.7	100.0	86.7	0.06	91	High-Ca Px [Diop]
28	TAM15-11	D8	1	*b.d.l*	0.2	*b.d.l*	15.6	12.5	35.4	*b.d.l*	0.2	*b.d.l*	*b.d.l*	*b.d.l*	*b.d.l*	36.1	100.0	84.3	1.36	45	Fayalite
29	TAM66-1	**B0**	**53**	**2.83**	**0.28**	**0.09**	**19.12**	**6.68**	**26.00**	**0.44**	**0.64**	**0.12**	**0.94**	**0.22**	**2.72**	**39.92**	**100.00**	**90.95**	**1.61**	**30**	**Bulk**
30	TAM66-1	B1	1	2.86	0.16	0.06	16.88	8.70	25.91	0.54	0.19	0.03	1.22	0.48	3.60	39.37	100.00	94.35	0.83	37	Matrix analyses
31	TAM66-1	B2	1	1.94	0.31	0.10	19.19	10.31	24.34	0.63	0.42	0.12	0.12	0.27	2.00	40.25	100.00	93.24	0.92	44	
32	TAM66-1	B3	1	1.66	0.05	0.07	13.74	7.00	36.66	4.00	0.13	0.05	0.06	0.03	1.48	35.08	100.00	104.67	0.76	49	
33	TAM66-1	B4	1	2.77	0.41	0.08	15.07	8.90	28.72	0.42	0.28	0.15	1.33	0.31	3.37	38.18	100.00	92.64	1.15	42	Fine-grained rim analyses
34	TAM66-1	B5	1	3.75	0.26	0.09	17.53	6.20	25.91	0.30	0.30	0.09	1.74	0.37	3.82	39.65	100.00	89.80	0.89	35	
35	TAM66-1	B6	1	3.42	0.24	0.09	15.75	7.43	29.05	0.29	0.21	0.10	1.36	0.17	3.42	38.46	100.00	92.17	1.11	37	
36	TAM66-1	B7	1	2.32	0.08	0.15	22.11	2.75	25.54	0.14	1.88	0.03	1.17	0.22	2.91	40.70	100.00	78.42	0.69	20	Altered chondrules
37	TAM66-1	B8	1	3.03	0.07	0.16	27.16	1.43	20.73	0.28	1.86	0.08	0.66	0.11	1.27	43.17	100.00	74.35	0.46	14	
38	TAM66-1	B9	1	*b.d.l*	0.3	*b.d.l*	20.6	20.6	25.5	0.2	0.3	*b.d.l*	*b.d.l*	*b.d.l*	*b.d.l*	32.5	100.0	82.5	0.74	65	Low-Ca Px [En]
39	TAM66-1	B10	1	1.50	8.69	0.24	23.16	12.62	8.79	0.06	0.51	0.07	0.26	0.01	0.74	43.36	100.00	97.94	0.23	77	High-Ca Px [Aug]
40	TAM66-1	B11	1	0.01	0.11	0.01	16.96	18.33	25.10	0.05	0.25	0.01	0.00	0.03	0.00	38.87	100.00	101.26	0.89	63	Fayalite
41	TAM66-1	B12	1	36.19	0.23	0.15	0.57	16.41	1.27	0.04	0.44	0.01	0.03	0.02	0.04	44.60	100.00	96.38	1.32	97	Mg-Al Spinel
42	TAM66-1	B13	1	36.8	*b.d.l*	0.4	0.8	16.8	3.2	*b.d.l*	3.5	*b.d.l*	0.1	*b.d.l*	*b.d.l*	38.6	100.0	80.4	2.46	92	

987

988 **Table.3.** Petrofabric analysis, circular statistics and entropy results.

989

No.	Sample	N=?	No. of fabrics	Entropy (S)	$S<S_{cutoff}$	Circ. Var	Circ. Kurtosis	Circ. Std. Dev.	Kappa (κ)
1	TAM19B-7	445	1	2.599	Positive	0.18	-11.25	36.41	1
2	TAM19B-17	48	1	2.688	Positive	0.24	-4.81	42.88	0.69
3	TAM19B-18	309	1	2.785	*Possible*	0.26	-3.84	44.61	0.62
4	TAM15-11	329	2	2.744	*Probable*	0.36	-1.73	54.56	0.33
5	TAM66-1	516	1	2.860	Negative	0.48	-0.28	65.36	0.15
6	Cold Bokkeveld	1054	1	2.619	*Reference value*	0.23	0.32	41.43	0.75
7	Jbilet Winsewlan	950	2	2.783	*Threshold value*	0.44	0.36	61.52	0.2

Fig.1. A) Particle TAM19B-7, a giant fine-grained micrometeorite. We show both the primary cross-sectioned (A-D, 830x950µm) and slices through additional fragments produced after the particle was crushed (E-H). The main cross-section (A-D) shows a well-defined geochemical boundary, separating two zones of distinct matrix, the larger "left hand" zone is Mg-bearing (4.1-8.2wt%), while the "right hand" portion is Mg depleted, with Mg concentrations below 3.0wt%. This region contains a circular inclusion, interpreted as a chondrule pseudomorph and highlighted by a dashed white square (B). The inclusion has a high porosity and is composed of phyllosilicate decomposition products. Its elliptical shape could indicate compaction during impact. There is also a compact, fine-grained rim [FGR] (C), approximately 15µm thick and containing Fe-Ni oxide nuggets surrounds the inclusion. The yellow A4 symbol denotes the position of a spot EDS analysis, shown in Table.2. A major element (Mg, Si, Fe) EDX map is shown in (D). In contrast, E-H show additional fragments, revealing a paucity of coarse-grained components throughout the particle. In H we have highlighted the tentative outline of a second possible pseudomorphic chondrule, similar to that shown in B and C. The stippled green lines in E and H mark where the initial cross-section cut through the particle.

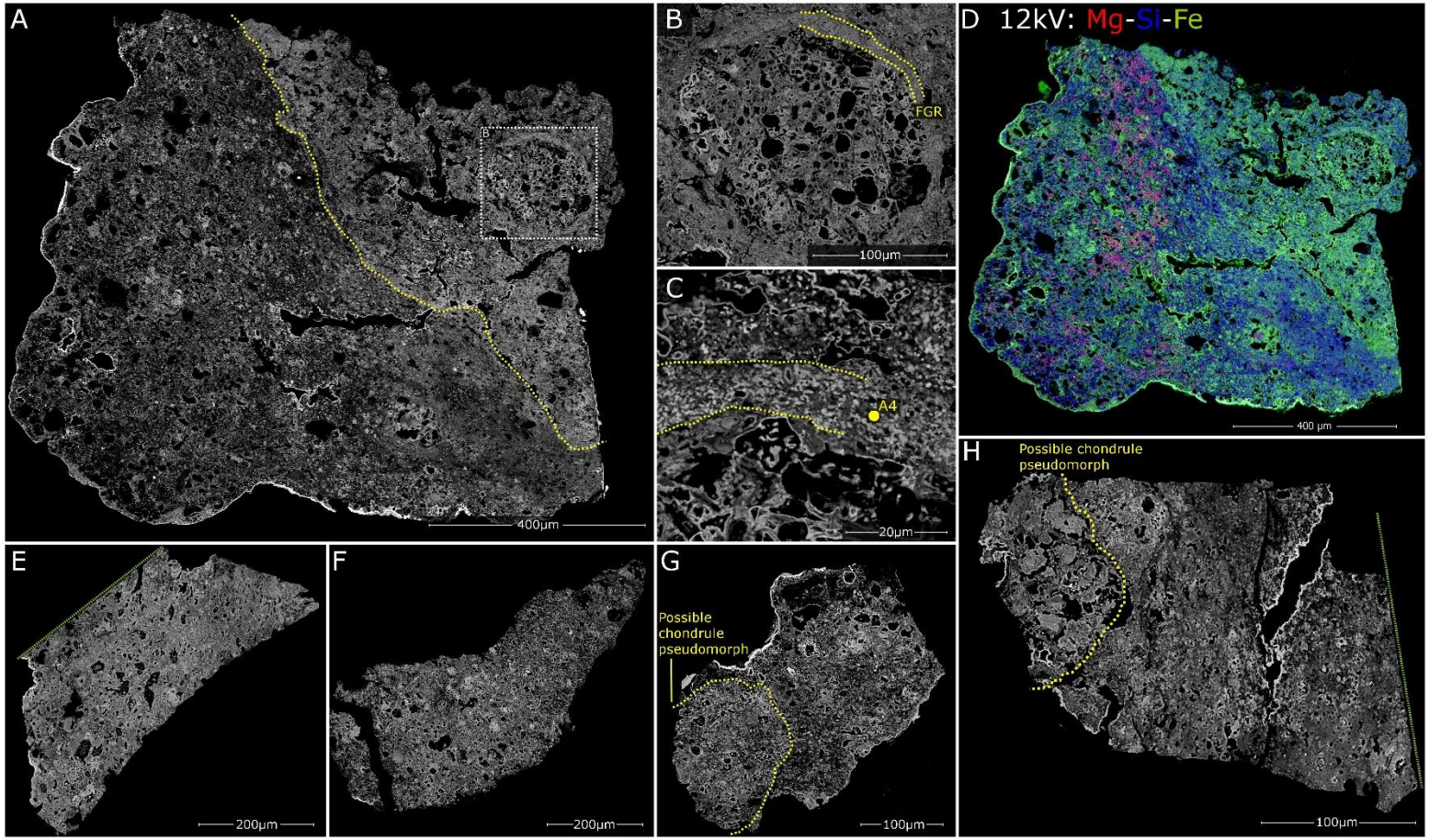

Fig.2. A) Particle TAM19B-17, this micrometeorite has a triangular cross-section and contains a compact, low-porosity and intensely aqueous altered internal texture. A thick jarosite encrustation rim surrounds the particle attesting to a significant period of terrestrial weathering. Inside the weathering encrustation is a magnetite rim, produced by atmospheric entry heating. The matrix contains a complex intermix of lighter (Fe-rich) and darker (Mg-rich) zones that are intergrown and cross cut by later periods of veining and pore-filling. Three regions are highlighted by a dashed yellow line, these indicate where refractory phases (silicates and oxides) have been partially altered and replaced, these zones are interpreted as ghost CAIs. Yellow dots B4-6 denote the locations of EDS spot analyses, shown in Table.2. Element maps (B and C) reveal the major element and trace refractory element distributions, and these aid in the identification of hydrated and partially replaced CAIs (D) and altered isolated anhydrous silicates (E).

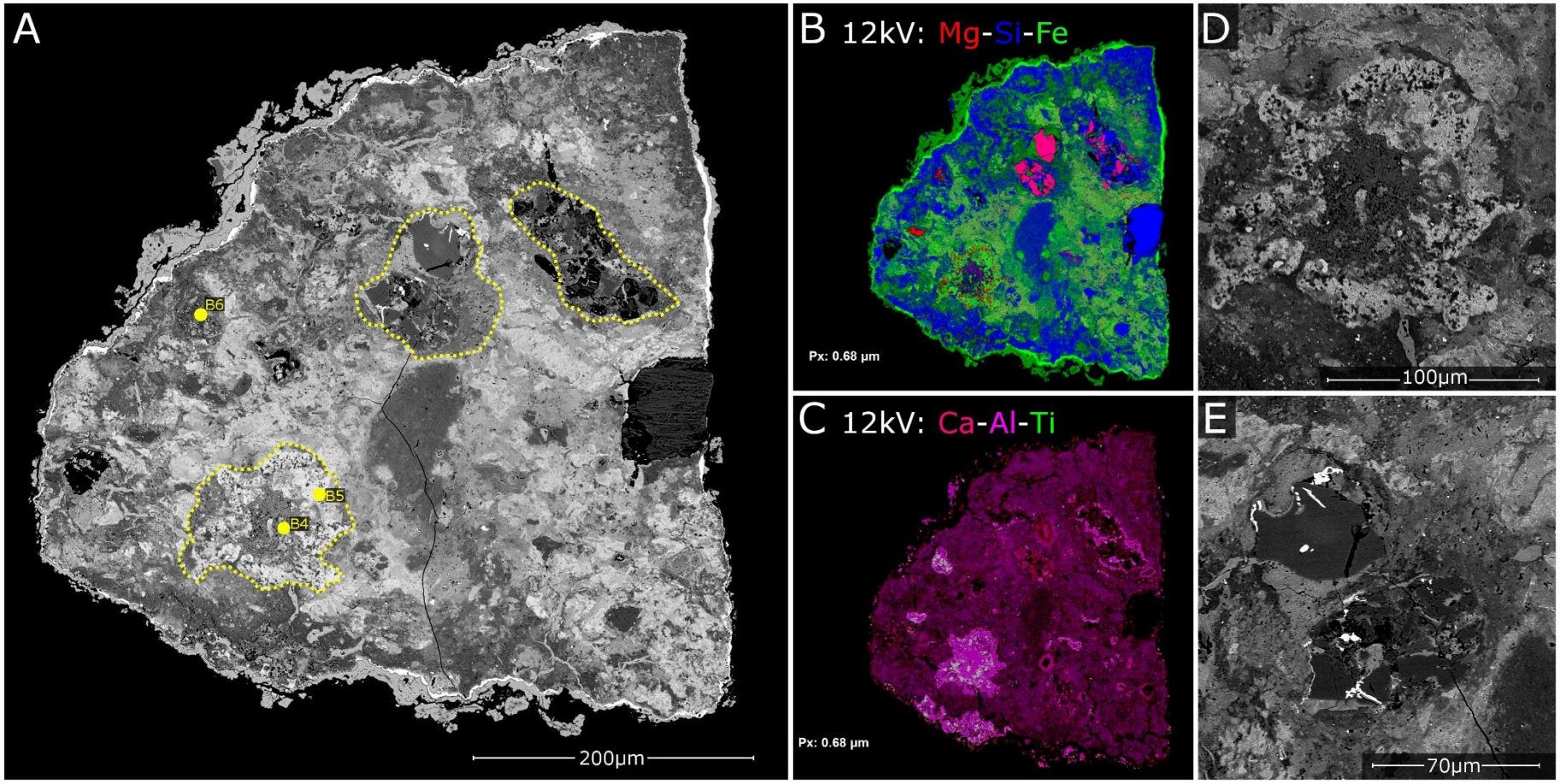

Fig.3. A) Particle TAM19B-18. This micrometeorite is composed of >85% matrix and is dominated by coarse, Fe-rich phyllosilicate decomposition products, which prior to atmospheric entry would have been cronstedtite (serpentine) clusters - equivalent to the PCP clumps described in previous studies of CM chondrites (Rubin et al., 2007). A lithic clast, composed of compact, Mg-rich matrix and containing a single large olivine crystal is found in the bottom right corner. The symbol C4-6 denote the location of an EDS spot analyses, shown in Table.1. (B, C, D and E) Anhydrous silicates are relatively rare and have anhedral rounded morphologies, containing abundant fractures, filled with serpentine alteration products, or are broken into a series of smaller, rounded and residual crystal relicts. Large phyllosilicate overgrowths mantle most grains, and in places generate a foliation texture, wrapping around larger crystals. Note: the view shown in (C) is from a higher plane of section and, therefore, cannot be located on the whole particle image, seen in (A). A major element (Mg, Si, Fe) EDX map is shown in (D).

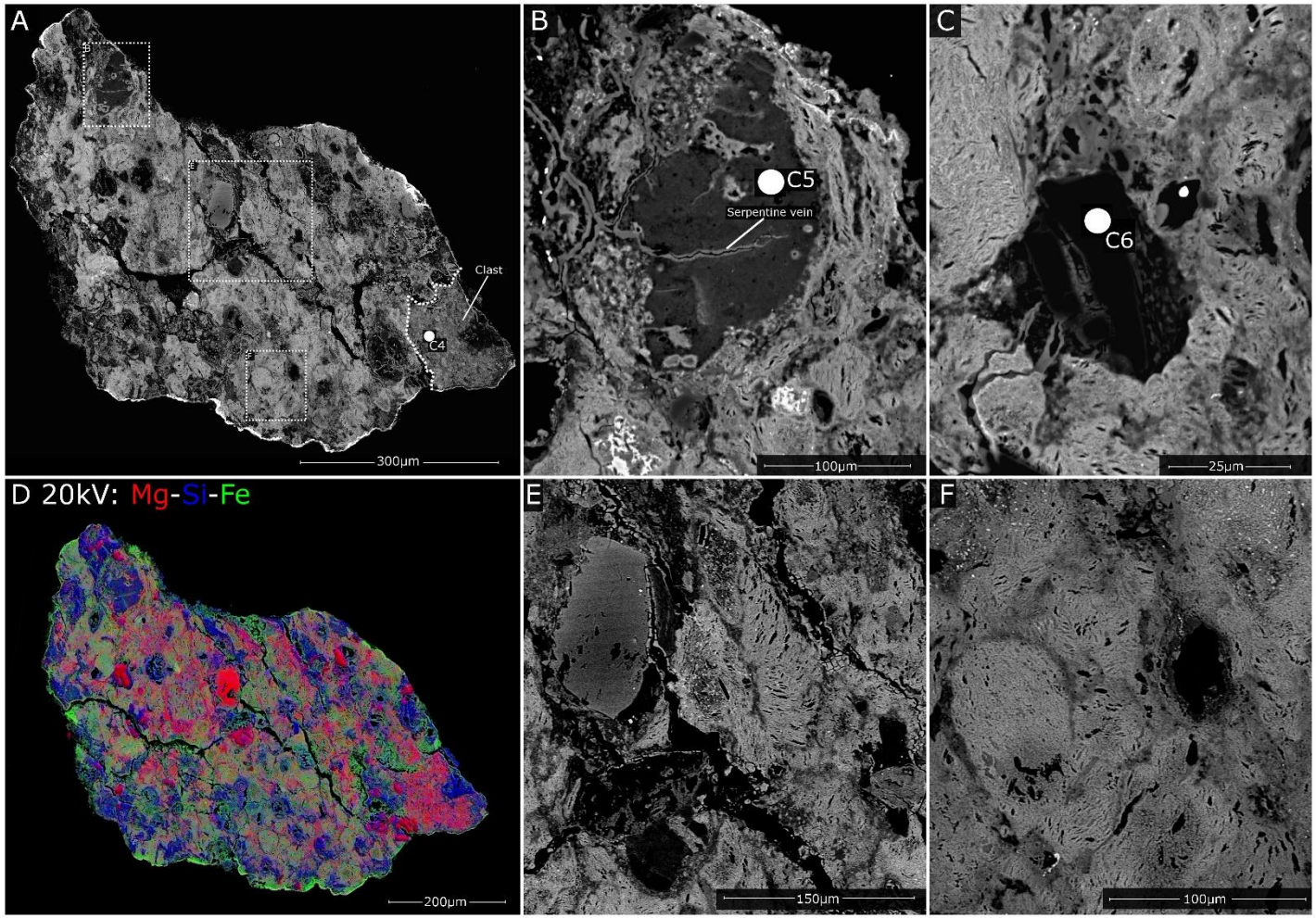

Fig.4. A) Particle TAM15-11 This micrometeorite has a broadly triangular cross-section, with a prominent magnetite rim. The internal mineralogy is dominated by (dehydroxylated) Fe-rich phyllosilicate. The right side of the particle (E) contains primarily coarse-grained phyllosilicate clusters with lozenge shapes, while the left side of the particle (G) is finer-grained, contains more Mg and preserves some fractured anhydrous silicate crystal relicts with low and high-Ca pyroxene compositions (C and D). The major element EDX map (B) demonstrates that the entire particle is Mg-poor, most likely reflecting the action of leaching during terrestrial weathering.

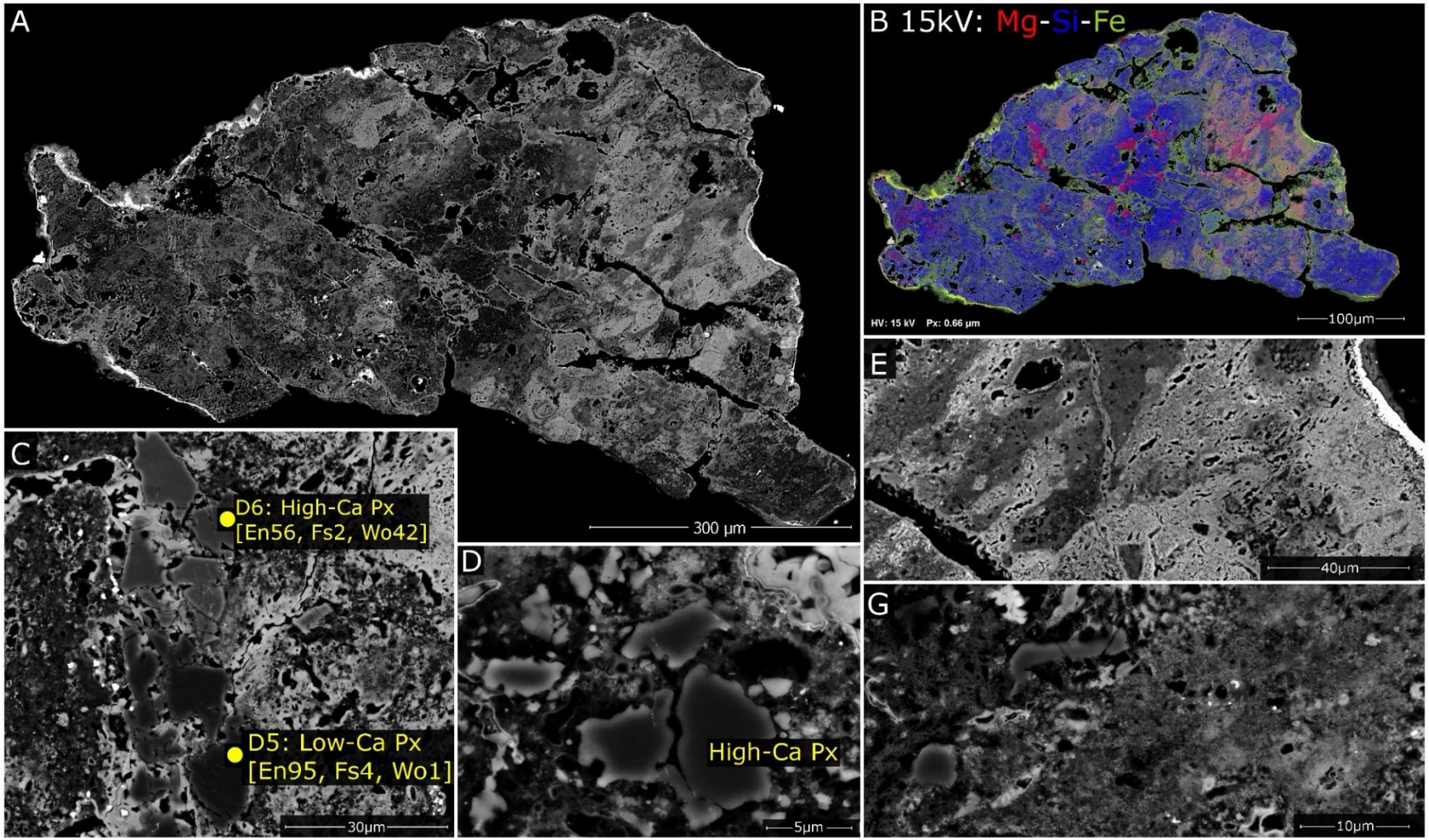

Fig.5. A) Particle TAM66-1, this micrometeorite is composed of Fe-rich vesicular matrix surrounding regions of darker, fine-grained Fe and Mg-poor matrix, as shown in the major element EDX map (B). In addition to the two large and approximately circular inclusions, which are easily distinguished and shown in C and F, several smaller zones of dark matrix are also surrounded by vesicular Fe-rich matrix, as shown in D and E. We interpret these circular regions as altered pseudomorphic chondrules, which originally had thick fine-grained rims (FGR). In contrast, the smaller dark inclusions represent phyllosilicate growth around isolated anhydrous silicate crystals and subsequent (partial) replacement. This particle texture, therefore, closely resembles the matrix of an intensely altered CM chondrites.

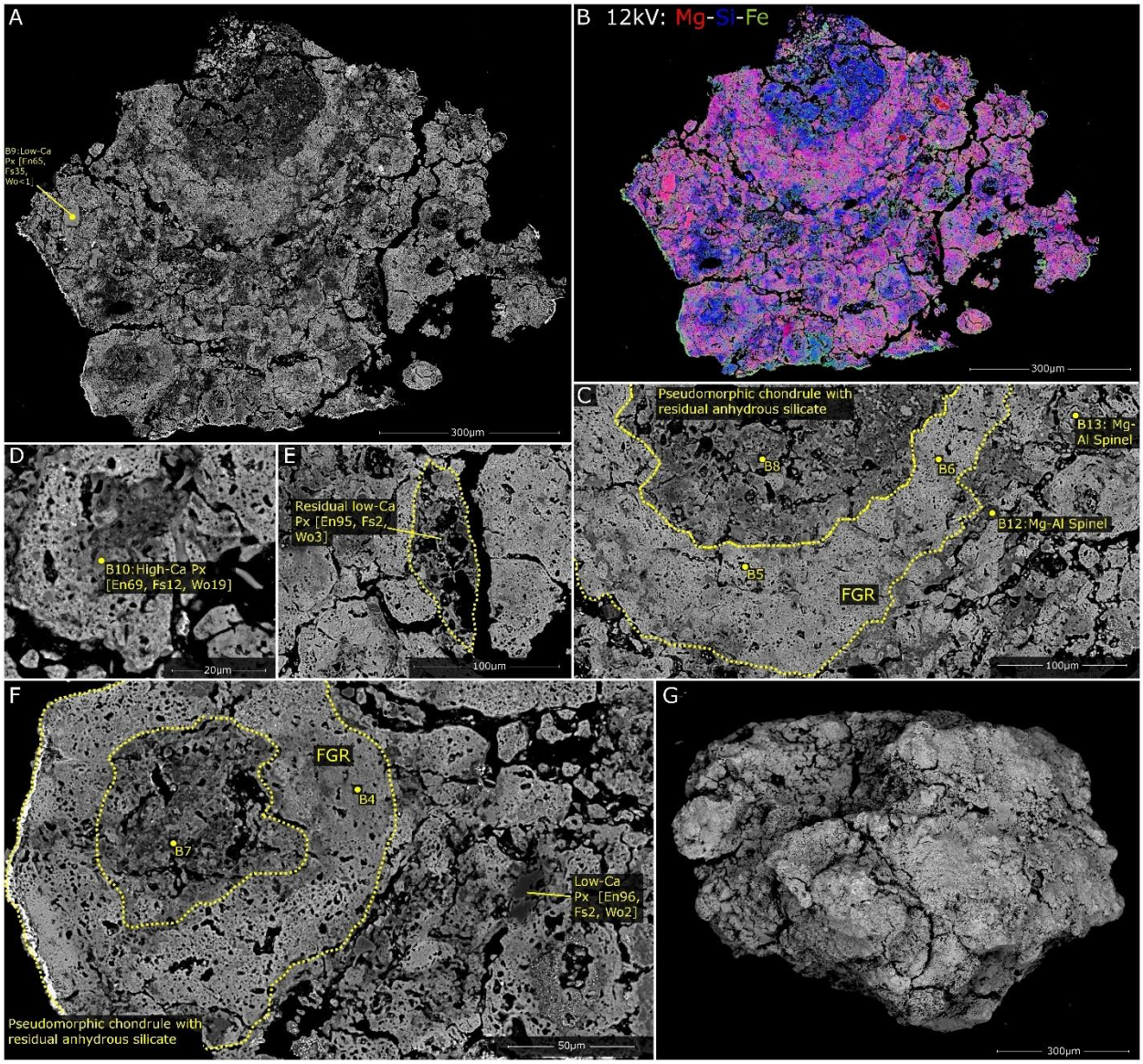

Fig.6. Micrometeorite matrix geochemistry: spider diagram showing elemental abundances for the five giant micrometeorites (TAM19B-18 [green], TAM19B-18 [black], TAM19B-7 [blue], TAM15-11 [dark green] and TAM66-1 [light green]) and the CM chondrite Mighei (a fresh fall) for reference. Elements are ordered by decreasing volatility, as defined by Lodders (2003) and normalized against CI carbonaceous chondrite values, obtained by analysis on a chip of Ivuna. These samples show a common abundance pattern, characteristic of the TAM micrometeorites. Samples are chondritic but with notable depletions in Ca (0.27-0.72), Mg (0.16-0.61), Ni (0.09-0.31), Co (b.d.l-0.28), Cu (b.d.l-0.91) and Zn (b.d.l-0.47). Meanwhile, particles are also significantly elevated in K, with concentrations between 10-25 times CI values. This pattern of depletions and enrichments is characteristic of the TAM micrometeorites and traces the effects of subaerial Antarctic terrestrial weathering on a chondritic sample (van Ginneken et al., 2016; Suttle et al., 2018).

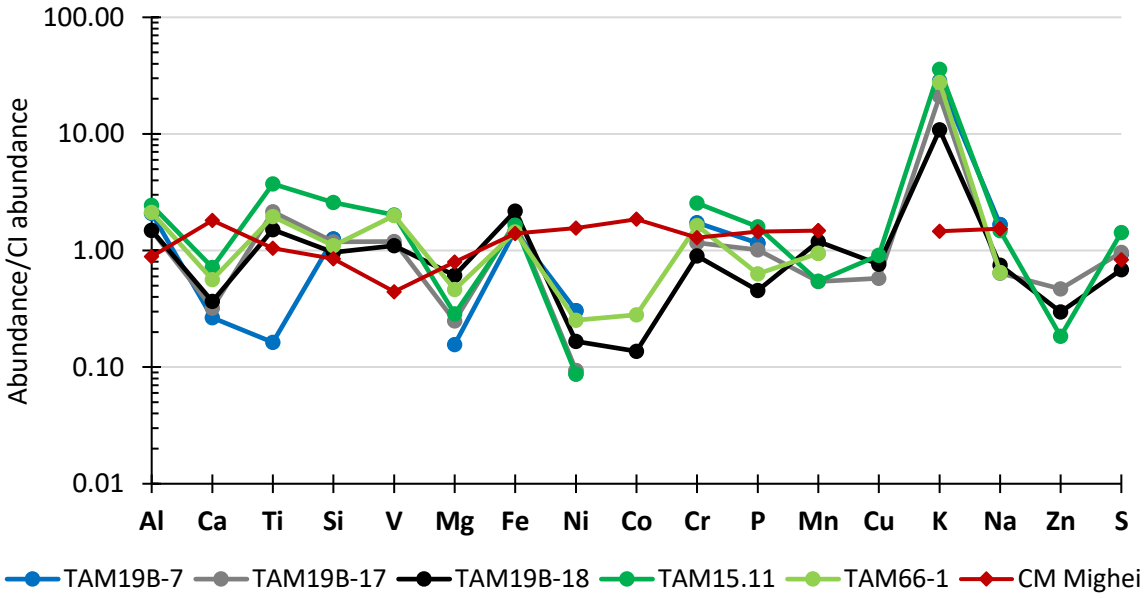

Fig.7. Micro-XRD patterns from TAM19B-17 (grey), TAM19B-18 (black) and TAM19B-7 (blue). Patterns are offset to aid interpretation. Major peaks associated with each mineral are marked using the following standard abbreviations: Fo=forsterite, En=enstatite, Aka=akaganéite, Cal=calcite, Hal=halite and Jar=jarosite. The last four minerals (Aka, Cal, Hal and Jar) are terrestrial weathering products, however, the presence of akaganéite implies the former existence of troilite and pyrrhotite, extraterrestrial Fe-Ni sulfide minerals. As with the spider diagrams, these XRD patterns are characteristic of TAM micrometeorites.

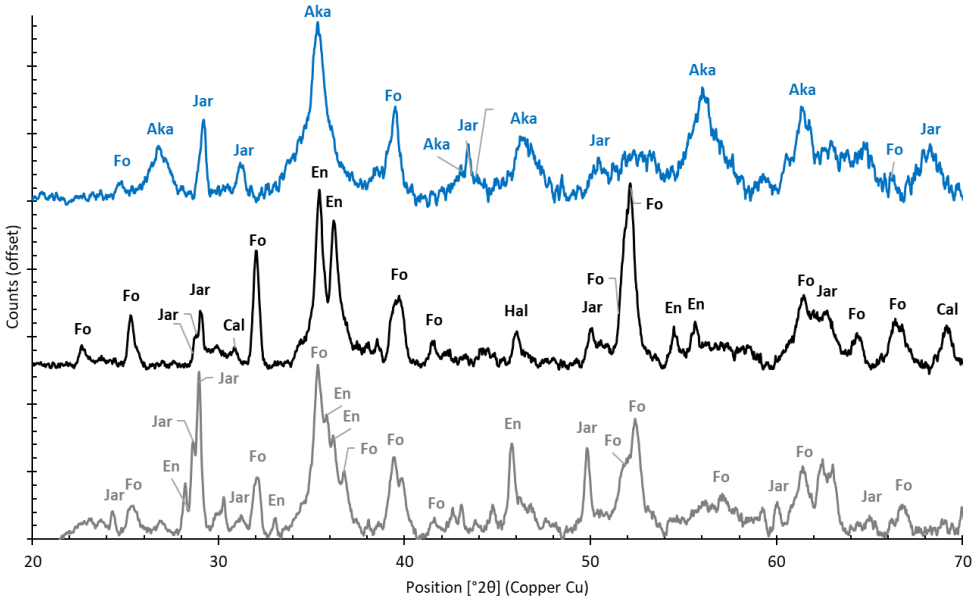

Fig.8. Micrometeorite matrix geochemistry (FeO/SiO_2 vs. Mg#) and inferred degree of alteration. The bulk matrix compositions of 77 small fine-grained Antarctic micrometeorites (FgMMs) from the Cap Prud'homme collection (previously analyses in Suttle et al. [2017a]) are used as a reference values to define an "*aqueous alteration trendline*". Reference values from several CM chondrites, CI Ivuna and the ungrouped meteorite C2 Tagish Lake are also shown. The matrix compositions for the five giant TAM micrometeorites are also plotted. The four open circles represent anomalously low Mg values and suggest Mg depletion during terrestrial weathering. Their corrected Mg# values are shown as solid circles. The TAM micrometeorites span a range of alteration degrees reflecting a similar range to the well-studied CM chondrites (Jbilet Winselwan to ALHA 81002). Error bars show 1 standard deviation from the micrometeorite's average matrix composition.

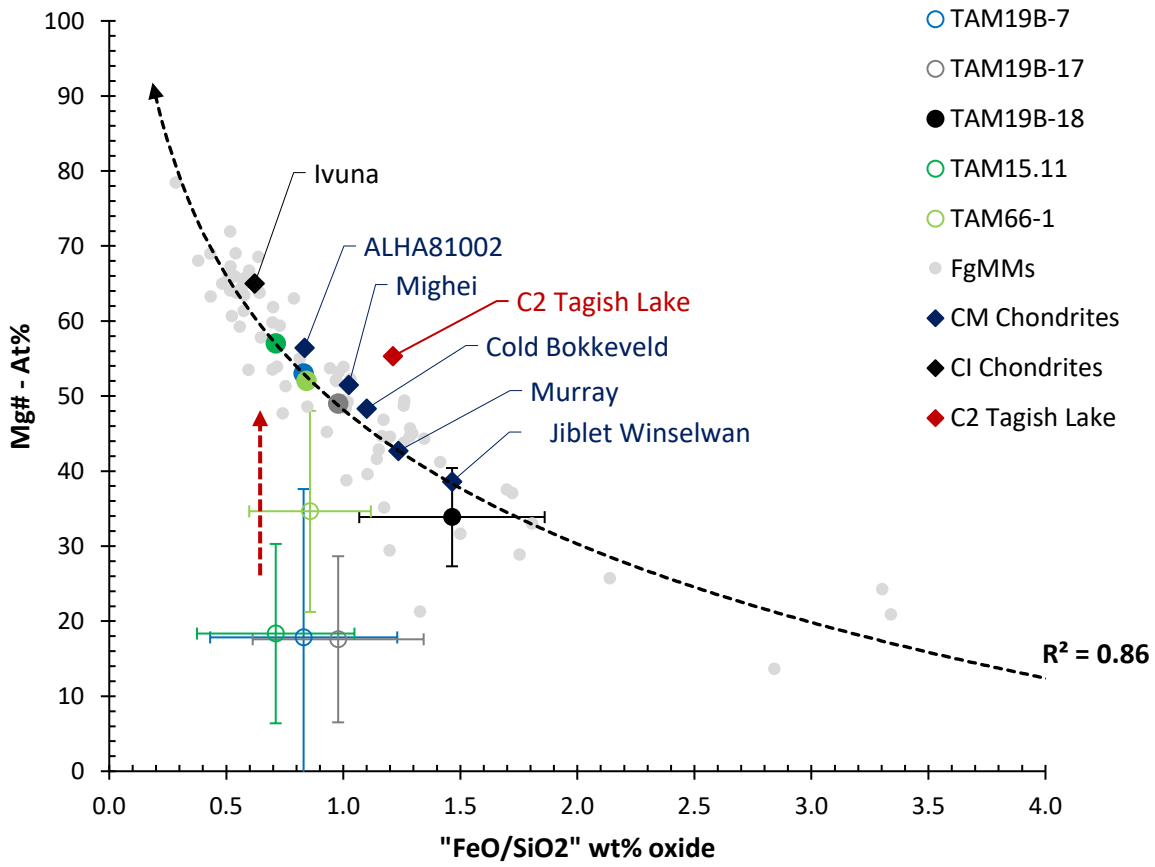

1062 **Fig.9**. Estimated phyllosilicate fraction and inferred petrologic subtype, modified after Howard et al., (2015)
1063 using data from CM, CR and ungrouped C2 chondrites. The five TAM micrometeorites (circled) have high
1064 phyllosilicate fractions (93-98%) suggesting low petrologic subtypes (<1.2) and, thus, intense alteration.

1065

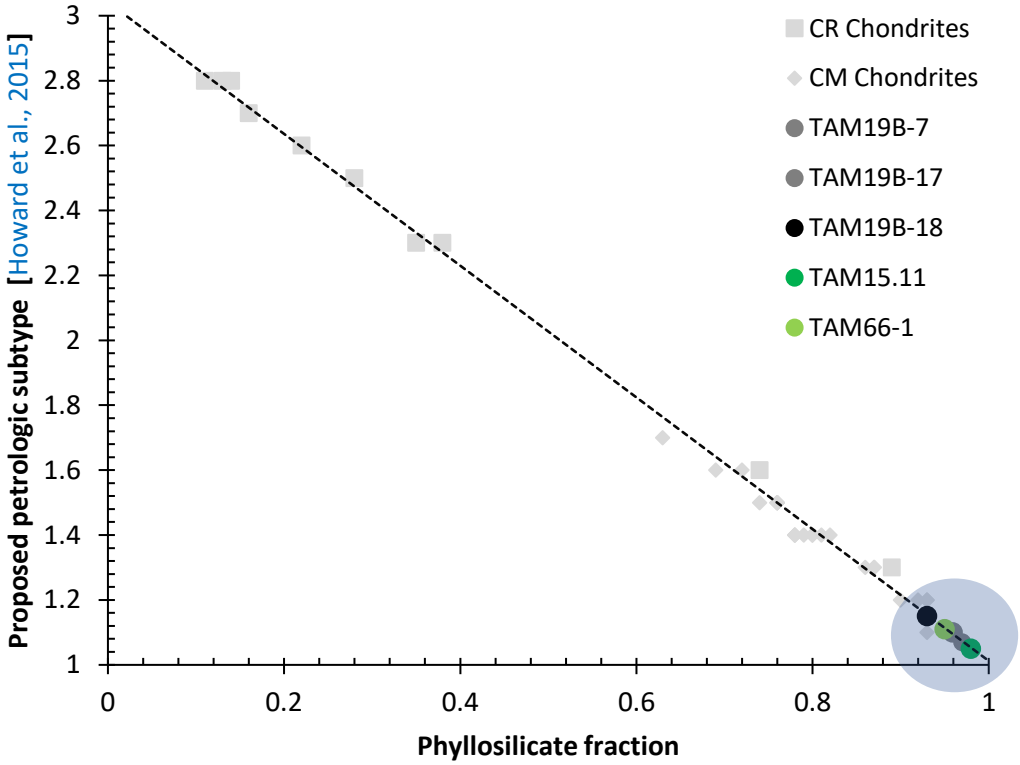

Fig.10. Petrofabric analysis, based on void orientations, using the method outlined in Suttle et al., (2017b). Voids were extracted from the BEI data and their orientation (long-axis) with respect to an arbitrary "north" recorded. A rose diagram of the void orientations (binned by 10° increments) was plotted and used to evaluate the presence or absence of a petrofabric. A strong uniaxial fabric is seen in TAM19B-7, this is also parallel to the elongation axis of the chondrule (shown by the dashed white line in the rose) suggesting both the matrix and chondrule are deformed in the same event, most likely an impact. Rose diagrams for the other four micrometeorites are also shown, three of which show evidence for a uniaxial fabric.